
Doctoral Dissertations

Student Theses and Dissertations

Summer 2022

Signal Integrity Analysis and Electromagnetic Inteference Modeling for Autonomous Vehicles

Yuandong Guo

Missouri University of Science and Technology

Follow this and additional works at: https://scholarsmine.mst.edu/doctoral_dissertations



Part of the [Electrical and Computer Engineering Commons](#)

Department: Electrical and Computer Engineering

Recommended Citation

Guo, Yuandong, "Signal Integrity Analysis and Electromagnetic Inteference Modeling for Autonomous Vehicles" (2022). *Doctoral Dissertations*. 3220.

https://scholarsmine.mst.edu/doctoral_dissertations/3220

This thesis is brought to you by Scholars' Mine, a service of the Missouri S&T Library and Learning Resources. This work is protected by U. S. Copyright Law. Unauthorized use including reproduction for redistribution requires the permission of the copyright holder. For more information, please contact scholarsmine@mst.edu.

SIGNAL INTEGRITY ANALYSIS AND ELECTROMAGNETIC INTERFERENCE
MODELING FOR AUTONOMOUS VEHICLES

by

YUANDONG GUO

A DISSERTATION

Presented to the Graduate Faculty of the
MISSOURI UNIVERSITY OF SCIENCE AND TECHNOLOGY

In Partial Fulfillment of the Requirements for the Degree

DOCTOR OF PHILOSOPHY

in

ELECTRICAL ENGINEERING

2022

Approved by:

Dr. Donghyun Kim, Advisor

Dr. Jun Fan

Dr. James Drewniak

Dr. Chulsoon Hwang

Dr. Shaowei Deng

© 2022

Yuandong Guo

All Rights Reserved

PUBLICATION DISSERTATION OPTION

This dissertation consists of the following three articles, formatted in the style used by the Missouri University of Science and Technology:

Paper I, found on pages 3–18, “Accurate and Broadband Three-Phase Motor Modeling Methodology Based on Vector Fitting”, has been submitted to *IEEE Transactions on Electromagnetic Compatibility*.

Paper II, found on pages 19–38, “Time-Efficient Worst-Case Glass-Weave Skew Estimation for Microstrip-Lines” has been submitted to *IEEE Transactions on Signal and Power Integrity*.

Paper III, found on pages 39–56, “A Comprehensive Study about Inhomogeneous Dielectric Layers (IDLs) and the Impacts on Far-End Crosstalk of High-Speed PCB Striplines”, has been published in the proceedings of *DesignCon 2022, Santa Clara, CA, USA, 2022*.

ABSTRACT

An autonomous vehicle (AV) may employ various sensors to detect the environment, and the hardware for self-driving should be able to process large volume of sensor data and make real-time decisions. For signal integrity (SI), both the bandwidths and data rates of the high-speed channels should meet the requirements. The electromagnetic interference (EMI) noise may become a major concern with the ever-increasing number of electric modules. This research focuses on both SI analysis and EMI modeling for AVs. The first topic is accurate and broadband three-phase motor modeling. The novel modeling methodology for a typical three-phase motor is presented, using which the motor characteristics can be reproduced. The second topic is related to SI and titled time-efficient worst-case glass weave skew (GWS) estimation for microstrip-lines. GWS is the dominant source of total line-to-line skew for differential signaling. Using the divide-and-conquer strategy, only the design information are needed for the calculations. Good correlation is reached, and it is more efficient to estimate the GWS. The third topic is titled a comprehensive study about inhomogeneous dielectric layers and the impacts on far-end crosstalk (FEXT) of high-speed PCB striplines. FEXT in PCB striplines is primarily attributed to dielectric inhomogeneity. The inhomogeneity problem is addressed by the novel algorithm that characterizes the D_k s of glass fibers and epoxy resin. Full-wave simulations and real-board measurements are conducted to verify the proposed approach.

ACKNOWLEDGMENTS

I would like to take this opportunity to express my sincere gratitude to Dr. Jun Fan, Dr. James Drewniak, Dr. David Pommerenke, Dr. Hongseok Kim, Dr. Chulsoon Hwang, and Dr. DongHyun Kim for the valuable help during my Ph. D. study. I really appreciate the instructions, training, encouragement, and guidance provided by them. I feel especially grateful to the mentoring provided by Dr. Jun Fan and Dr. Hongseok Kim, which helped building me strong critical-thinking and research skills.

I also would like to thank Dr. DongHyun Kim and Dr. Shaowei Deng for offering me the great internship opportunities, which helped broaden my horizon and paved my future professional career path. Special thanks to Dr. Xiaoning Ye, although he is not in the committee, for the insightful comments, brilliant ideas, and helpful discussions during the last five years.

I want to thank my wife, Wen Yang, for the unconditional love and support for me and the family, which made my Ph. D. study possible. I also want to thank my parents and my two lovely daughters for their patience. I am sorry for the limited family time which I could join during my Ph. D. study.

This dissertation is based upon work supported partially by the National Science Foundation under Grant No. IIP-1916535, Intel Corporation, and Huwin Co., Ltd.

TABLE OF CONTENTS

	Page
PUBLICATION DISSERTATION OPTION	iii
ABSTRACT.....	iv
ACKNOWLEDGMENTS	v
LIST OF ILLUSTRATIONS.....	ix
LIST OF TABLES	xii
 SECTION	
1. INTRODUCTION.....	1
 PAPER	
I. ACCURATE AND BROADBAND THREE-PHASE MOTOR MODELING METHODOLOGY BASED ON VECTOR FITTING	3
ABSTRACT	3
1. INTRODUCTION.....	4
2. INTRODUCTION TO THE VECTOR FITTING METHOD AND THE PMSM UNDER STUDY.....	7
3. MOTOR MODELING IN THE LOW FREQUENCY BAND	9
4. MOTOR MODELING IN THE HIGH FREQUENCY BAND.....	14
5. CONCLUSION	16
REFERENCES	16
II. TIME-EFFICIENT WORST-CASE GLASS-WEAVE SKEW ESTIMA- TION FOR MICROSTRIP-LINES	19
ABSTRACT	19

1. INTRODUCTION.....	20
2. MODELING STRATEGY.....	23
2.1. OVERALL MODELING STRATEGY: DIVIDE AND CONQUER.....	23
2.2. THE INFLUENCE OF COUPLING TERMS ON GWS.....	23
3. DETERMINATION OF LOCAL DK VALUES.....	27
4. VALIDATIONS AND DISCUSSION.....	31
4.1. COMPARISON OF GWS WITH DIFFERENT TRACE LOCATIONS	31
4.2. COMPARISON OF GWS WITH DIFFERENT TRACE ROTATION ANGLES	32
4.3. COMPARISON OF TIME CONSUMPTIONS	34
4.4. DISCUSSION.....	35
5. CONCLUSION	35
APPENDIX	36
REFERENCES	36
III. A COMPREHENSIVE STUDY ABOUT INHOMOGENEOUS DIELEC- TRIC LAYERS (IDLS) AND THE IMPACTS ON FAR-END CROSS- TALK OF HIGH-SPEED PCB STRIPLINES	39
ABSTRACT	39
1. INTRODUCTION.....	39
2. REPRESENTATION OF IDLS WITH GLASS AND RESIN LAYERS	42
3. CALCULATIONS OF DK VALUES OF CORE AND PREPREG.....	43
4. EXTRACTION OF DK VALUES OF GLASS AND RESIN.....	47
5. MEASUREMENT-BASED VALIDATION	48
6. IMPACT OF GEOMETRICAL PARAMETERS ON STRIPLINE FEXT	50

6.1. EFFECT OF GLASS LAYER POSITION ON FEXT	51
6.2. EFFECT OF GLASS LAYER THICKNESS ON FEXT	53
7. CONCLUSION	54
REFERENCES	55
SECTION	
2. CONCLUSIONS	57
BIBLIOGRAPHY	58
VITA	60

LIST OF ILLUSTRATIONS

	Page
 PAPER I	
Figure 1. The illustration of the internal structure of the PMSM under study	9
Figure 2. The flowchart of the motor modeling process.....	10
Figure 3. The sketches of the motor configurations for: (a) CM impedance measurement, (b) DM impedance measurement	10
Figure 4. The demonstration of the good agreements between the vector fitting results and measurement data in the comparisons of: (a) DM admittance magnitude, (b) DM admittance phase. The deviations in (a) are in the range of 10^{-5} to 10^{-1} when the fitting order is 5.	11
Figure 5. The generated one-port equivalent circuit model through the vector fitting method and based on the measured motor DM admittance.	12
Figure 6. The comparisons between the simulation results obtained through the circuit model shown in Figure 7 and the measurement data: (a) CM impedance magnitude comparison, (b) CM impedance phase comparison.....	13
Figure 7. The equivalent circuit model considering both motor CM and DM characteristics in the low frequency band.....	13
Figure 8. The representation of the arrangement at the motor terminals during the S-parameter measurements	14
Figure 9. The generated motor SPICE model in the frequency range of DC to 120MHz	14
Figure 10. Verification of the constructed motor SPICE model through the comparison of motor DM impedance: (a) DM impedance magnitude, (b) DM impedance phase	15
Figure 11. Verification of the constructed motor SPICE model through the comparison of motor CM impedance: (a) CM impedance magnitude, (b) CM impedance phase..	15

PAPER II

Figure 1. Illustration of the differential microstrip-line under study: (a) the top view and demonstration of trace segmentation, (b) a simplified cross-section showing the definitions of geometrical parameters.	24
Figure 2. Full-wave simulation-based study: (a) comparison of calculated GWS to reveal the impact of coupling terms, (b) comparison of insertion loss and FEXT magnitudes, which indicates that the coupling terms can be ignored in GWS calculations.	27
Figure 3. Cross-sections that are used for determination of local D_k values: (a) for the segments in the first category (segments i and j in Figure 1 (a)), (b) for the segments in the second category (segment k in Figure 1 (a)).	29
Figure 4. Top-view sketch of the microstrip-lines in the full-wave simulations and demonstration of how trace location is swept with the illustrations of start point, end point, and sweeping direction	32
Figure 5. Comparison of GWS when manipulating signal trace locations. Good correlation is achieved	33
Figure 6. Illustration of how trace-rotation angle is changed through the top view of the microstrip-lines in the simulations.....	33
Figure 7. Comparison of GWS when manipulating signal-rotation angle. Good agreement is reached.....	34

PAPER III

Figure 1. Cross-sectional image of two coupled single-ended striplines, obtained by scanning electron microscopy.....	41
Figure 2. Representation of the stripline cross-section shown in Figure 1 using equivalent glass and resin layers.....	42
Figure 3. Existing models for describing material inhomogeneity and predicting stripline FEXT..	43
Figure 4. Cross-section of a single-ended stripline with inhomogeneous materials.....	44
Figure 5. Two additional models created for determining Dk_{core} and Dk_{preg} based on Dk_{glass} and Dk_{resin}	46

Figure 6. Measured modal S-parameters (insertion loss).	49
Figure 7. Cross-section of the testing vehicle.	50
Figure 8. Comparison of time-domain FEXT.	51
Figure 9. 2D model used to study the impact of glass layer location on stripline FEXT.	52
Figure 10. Comparison of simulated FEXT in the time domain when the glass layer location is swept.	53
Figure 11. Comparison of simulated FEXT in the time domain for varying glass layer thickness.	54
Figure 12. Comparison of simulated TDR impedance for varying glass layer thickness.	54

LIST OF TABLES

	Page
 PAPER I	
Table 1. The Equivalent Circuit Model When $f(s)$ is the Input Impedance.....	8
Table 2. The Equivalent Circuit Model When $f(s)$ is the Input Admittance.....	8
Table 3. Values of the Poles, Residues, and Constants in the Vector Fitting.....	11
Table 4. Component Values in the Circuit Model in Figure 5.....	12
 PAPER II	
Table 1. Values of Geometrical Parameters.	25
Table 2. Server Hardware Settings.	34
Table 3. Comparison of Time Consumption.....	35
 PAPER III	
Table 1. Thickness of Glass and Resin Layers.	50
Table 2. Extracted Dk Values at 1GHz.....	50
Table 3. Cross-Sectional Geometries in Figure 9.	52
Table 4. Material Properties in Figure 9.	52

SECTION

1. INTRODUCTION

An autonomous vehicle (AV) may employ many kinds of sensors in order to detect the environment, and the AV technology has been applied to electric vehicles. Therefore, both the high-speed modules and power electronics modules are integrated inside an AV. The hardware for self-driving should be able to process large volume of sensor data and make real-time driving decisions. From signal integrity (SI) perspective, both the bandwidth and transition speed of the high-speed channels should meet the requirements. With various electric modules incorporated, the electromagnetic interference (EMI) noise may become a major concern, as EMI issues may undermine the performances of these modules and may even threaten the safety of the passengers. Autonomous vehicles provide plenty of opportunities for technology innovations in the SI and EMI areas. However, the associated design may be quite challenging [1]-[3].

The induced electromagnetic interference (EMI) noises in a three-phase motor-drive system may have adverse impacts on the functionality of adjacent electronic devices [4]. An accurate and broadband three-phase motor model would be desired for the study of EMI behaviors of the motor-drive system. However, there is no previous work showing accurate result if the frequency range of interest includes the frequency-modulation band. The novel modeling methodology for a typical permanent magnet synchronous motor (PMSM) in a vehicular three-phase braking system is presented herein, using which the motor common- and differential-mode characteristics can be

reproduced with high accuracy in the frequency range of 1 Hz to 120 MHz [5]. In addition, the unbalanced nature among the three phases of the PMSM under study, which cannot be captured using any known modeling approaches, is able to be regenerated.

Glass-weave skew (GWS), resulting from varying dielectric constant around the signal trace, is dominant source of total line-to-line skew in differential signaling. The relative locations between signal conductors and glass fibers are random in real printed circuit boards, which introduces significant uncertainty in the resulting GWS [6]-[10]. Thus, it is desired to develop a feasible methodology for worst-case GWS prediction, so that engineers can evaluate their high-speed designs. However, due to the statistical characteristic of GWS problems and complexity involved in the inhomogeneous dielectric [11]-[17], predicting the worst-case scenario is regarded as a challenging task. The traditional GWS evaluation methods require either full-wave simulations or measurements of numerous test vehicles, which is time-consuming. Herein, a time-efficient approach for worst-case estimation of GWS is presented and applicable to microstrip-lines.

Far-end crosstalk (FEXT) in typical high-speed PCB striplines is primarily attributed to dielectric inhomogeneity. In this paper, the inhomogeneity problem is comprehensively addressed by a novel algorithm that characterizes the dielectric constants (Dk s) of glass fibers and epoxy resin. In contrast to other methods, the proposed approach enables one to assess the impact of geometrical parameters on stripline FEXT and to estimate Dk_{core} and $Dk_{prepreg}$ based on Dk_{glass} and Dk_{resin} values extracted through analytical expressions. Full-wave simulations and real-board measurements are conducted to verify the proposed approach.

PAPER

I. ACCURATE AND BROADBAND THREE-PHASE MOTOR MODELING METHODOLOGY BASED ON VECTOR FITTING

Y. Guo

Department of Electrical Engineering, Missouri University of Science and Technology,
Rolla, MO 65409

Email: ydggdd@umsystem.edu

ABSTRACT

An accurate and broadband modeling methodology for a typical permanent magnet synchronous motor (PMSM) in a vehicular three-phase braking system is proposed for the first time to improve the accuracy of induced electromagnetic interference (EMI) in three-phase motor systems. The proposed model is verified by measurement from DC to 120 MHz both in common-mode and differential-mode current measurement of the three-phase motor under study. and the proposed model can be used in analysis and prediction of the electromagnetic noise of the motor-drive braking system. The model can also be incorporated into frequency- and time-domain simulations. The modeling approach is based on vector fitting technique of measured three-phase motor impedance and S-parameter, where the three-phase PMSM is modeled as a multi-port device. In addition, the proposed modeling method for the PMSM can be used for different types of three-phase motors for EMI simulations and analysis.

Keywords: broadband modeling, common mode, differential mode, electromagnetic interference, impedance measurement, motor drive system, mode transformation, three-phase motor, vehicle braking system, vector fitting method.

1. INTRODUCTION

The three-phase electric drive systems are widely utilized in the electric vehicles (EVs). The induced electromagnetic interference (EMI) noises in the three-phase motor-drive systems due to the fast switching of the semiconductors would propagate and radiate internally and externally, which adversely affect the functionality and performances of the electronic components and devices inside and outside an EV [1]. In order to analyze and predict the EMI behavior of a three-phase motor-drive system quantitatively and qualitatively, it is necessary to construct an accurate EMI model for the three-phase motor under study.

The experiment methods and requirements of the radio electromagnetic disturbance generated by a vehicular motor-drive system are described and standardized in CISPR 25 [2], where the frequency ranges of the EMI measurements for conducted and radiated emissions cover both AM and FM bands in which the limits are extremely low for the effective protection of an on-board AM and/or FM radio receiver. This necessitates a broadband three-phase motor model in the associated simulation-based studies.

Conventionally, the EMI problems in a motor-drive system are oftentimes attributed to the common mode (CM) noise [3]-[7]. However, as indicated and studied in

[8]-[12], the mode transformation between the CM and differential mode (DM) noises could occur due to the imbalances in either the printed circuit board structure or the EMI filter design. Therefore, a time-domain simulation technique would be adopted for the EMI modeling of a motor-drive system, which requires the three-phase motor model can function from DC.

Considerable effort has been devoted in the three-phase motor modeling. The high-frequency equivalent circuit models for the three-phase induction motors presented in the pioneering work are constructed with the concentration on the CM noise propagation paths [13], [14]. A CM circuit model is proposed in [4] and is dedicated for the permanent magnet synchronous motor (PMSM) under study in the frequency range of 10 kHz to 20 MHz. A more comprehensive circuit model of a three-phase induction motor enabling both CM and DM simulations is demonstrated in [15], where the parameterization technique is also introduced. However, the proposed model in [15] only works up to 30 MHz with limited accuracy around all the resonance frequencies and in the frequency range beyond roughly 12 MHz. The analogous equivalent circuit models considered as the simplified version of the one in [15] are exhibited in [3] and [16]. The modeling approaches for a three-phase AC motor are explored in [17], and the associated pros and cons of the corresponding physical models, behavior models, and the transmission line and T models are explained and compared.

The vector fitting is a promising methodology which can generate wide-band and high-accuracy rational models due to its robust and efficient formulation [18], [19]. The vector fitting method has been applied in various areas including the modeling of a three-phase motor. An equivalent circuit model is established in [1] based on the vector fitting

scheme to manifest the motor CM behavior. The vector fitting procedure for the modeling of measured motor CM and DM impedances are described in [20] and [21], in which the frequency ranges are 10 kHz to 40 MHz and 100 kHz to 100 MHz, respectively. The motors in [20] and [21] are considered as a one-port device so that the vector fitting mechanism is applied twice in the modeling process for the generation of the CM and DM circuit models separately.

The PMSMs are gaining their popularity in recent years in the hydraulic pressure control of the vehicular motor-drive braking systems thanks to the characteristics of the high power density and high torque/inertia ratio [4], [6]. Due to the wide applications and the high current nature, the analysis and estimation of the induced EMI from a motor-drive system where a PMSM is utilized becomes essential and more challenging.

In this paper, a typical PMSM is modeled and an accurate broadband SPICE model is built upon the vector fitting method, where a systematic modeling methodology is also demonstrated. The whole frequency range, which is DC to 120 MHz, is divided into two bands in this study, namely, the low frequency band below 1 MHz and the high frequency band 1 MHz to 120 MHz. The motor impedance and associated S-parameters are measured in the low and high frequency ranges respectively, and the PMSM under study is regarded not only as a one-port but also a multi-port device during the measurements. The SPICE model is developed based upon the constructed S-parameters covering the entire frequency range of interest. Therefore, the model is able to be integrated into both frequency- and time-domain simulations as it can regenerate the CM and DM characteristics of the PMSM perfectly. In addition, the proposed modeling method can be extended and applied to the three-phase motors of other types since none

of the PMSM-related conditions and assumptions have been involved during the model development.

2. INTRODUCTION TO THE VECTOR FITTING METHOD AND PMSM UNDER STUDY

The vector fitting approximates a frequency response $f(s)$ with a rational function and the general expression is [18], [19]:

$$f(s) \approx \sum_{n=1}^N \frac{c_n}{s-a_n} + d + s \cdot e. \quad (1)$$

where, c_n and a_n are the residues and poles, respectively. The coefficient d is constant and e is a real number. The residues and poles could be real-valued numbers or complex-valued conjugate pairs, or a combination of two, depending on whether there are resonance peaks and/or valleys in the target functions. In general, the deviations between the target function and the fitted one tend to get smaller for a larger fitting order n . The function $f(s)$ can be solved by finding the coefficients with respect to the responses at the given frequencies through the least square method [1]. The real initial poles could be employed in the vector fitting process for smooth target functions, which can help accelerate the iterations and simplify the constructed equivalent circuit model.

Assuming the input impedance is measured for a single-port device and treated as the goal function for vector fitting, the equivalent circuit models for the real poles, the constant d as well as the real-valued parameter e are summarized in Table 1 and Table 2 [22], [23]. The circuit models for the conjugate complex poles are excluded in this paper but are available in [20] and [21], since only the real poles are adopted in fitting the

PMSM characteristics in the aforementioned low frequency band where the “smooth function” condition is satisfied.

Table 1. The Equivalent Circuit Model When $f(s)$ is the Input Impedance

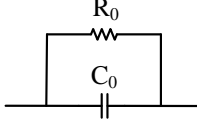
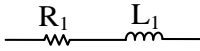
Expression	Equivalent Circuit Model	Parameterization
$\frac{c_n}{s - a_n}$		$R_0 = -\frac{c_n}{a_n}$ $C_0 = \frac{1}{c_n}$
$d + s \cdot e$		$R_1 = d$ $L_1 = e$

Table 2. The Equivalent Circuit Model When $f(s)$ is the Input Admittance

	f_1	f_2	m_1	m_2	$\Delta\epsilon'$	ϵ'_∞
ϵ_{d1}	1 kHz	10 THz	3.80	13.80	0.12	3.21
ϵ_{d2}	30 GHz	10 THz	11.28	13.80	0.04	0.08

In this paper, the three-phase PMSM in the motor-drive braking system employs the delta-connection topology in its stator coil and permanent magnet in its rotor. The PMSM and the three-phase AC busbars are integrated into a metal housing which is considered as one critical element for the CM noise propagation. The internal structure of the PMSM is illustrated in Figure 1 after removing the AC busbars and motor housing.

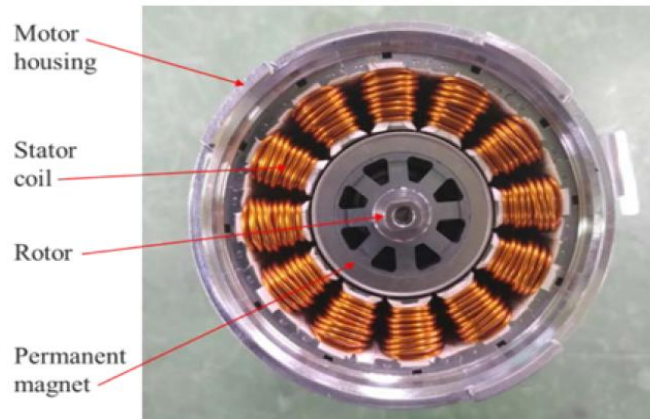


Figure 1. The illustration of the internal structure of the PMSM under study.

3. MOTOR MODELING IN THE LOW FREQUENCY BAND

The developed SPICE model of the PMSM under study through the vector fitting method is based on the S-parameters from DC to 120 MHz. The flowchart of the systematic motor modeling methodology in the whole frequency range of interest is illustrated in Figure 2. However, a VNA is generally not suitable for the ultralow-frequency measurements. The modeling process in the low frequency band is documented in this section, where the impedance analyzer Keysight E4990A-120 and the impedance probe kit Keysight 42941A are adopted for the motor CM and DM impedance measurements in the frequency range of 20 Hz to 1 MHz. The motor terminal configurations are sketched in Figure 3.

In order to avoid the incorporations of the negative resistance or inductance in the constructed equivalent circuit model, the measured motor DM impedance is converted to the DM admittance before the application of vector fitting.

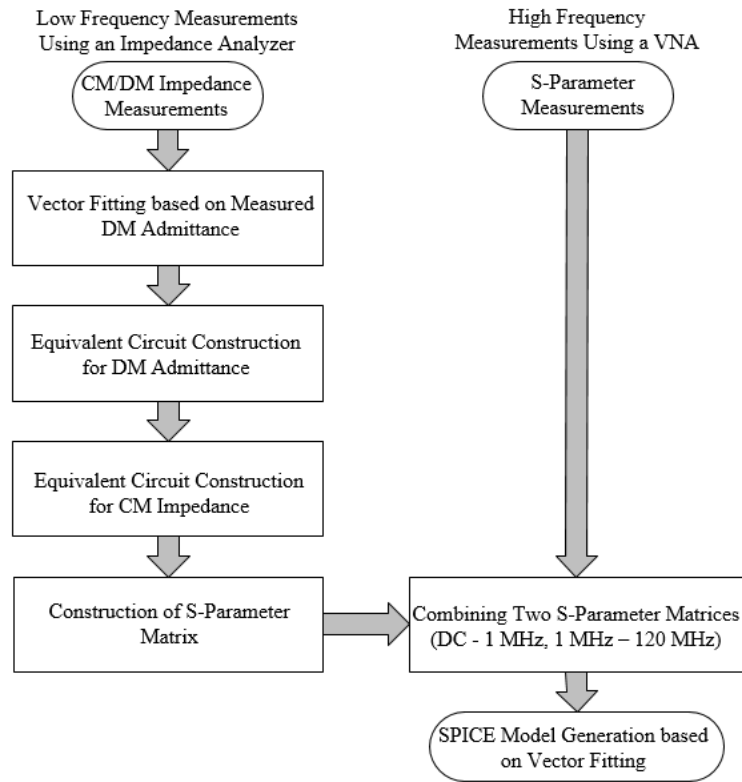


Figure 2. The flowchart of the motor modeling process.

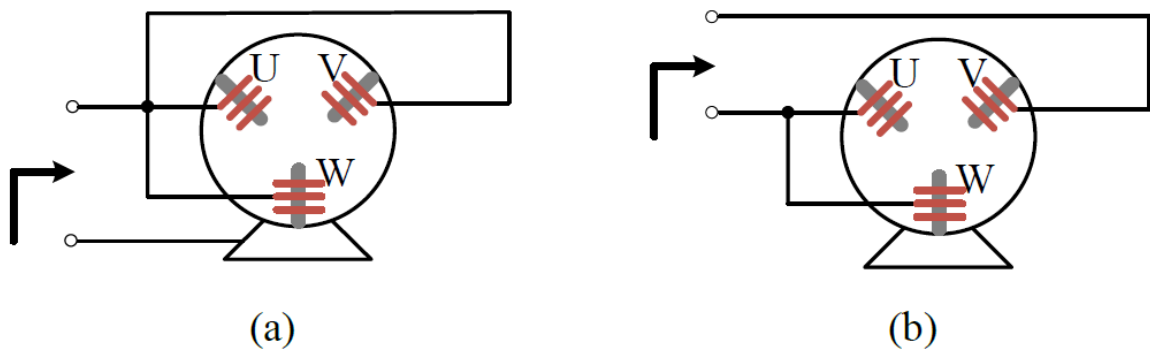


Figure 3. The sketches of the motor configurations for: (a) CM impedance measurement, (b) DM impedance measurement.

It is found that the good correlations exhibited in Figure 4 can be achieved in both DM admittance magnitude and phase comparisons when the fitting order is 5. Table 3 summarizes the coefficient values in (1) obtained through the vector fitting. The

generated one-port circuit model is demonstrated in Figure 5 with the circuit component values listed in Table 4.

Table 3. Values of Poles, Residues, and the Constants in the Vector Fitting

n	Poles (a_n)	Residues (c_n)	d	e
1	-3.7776×10^6	4.7486×10^4	0.0062	1.2369×10^{-11}
2	-0.4150×10^6	2.1009×10^4		
3	-0.432×10^5	3.3786×10^3		
4	-0.1×10^4	2.2315×10^4		
5	-0.6×10^3	1.6477×10^3		

Assuming a balanced structure for the PMSM under study, the equivalent circuit model with the three terminals, namely, terminals U, V, and W, can be readily attained based upon the one-port circuit model shown in Figure 5, in which all the resistance, inductance and capacitance are doubled compared to the values in Table 4.

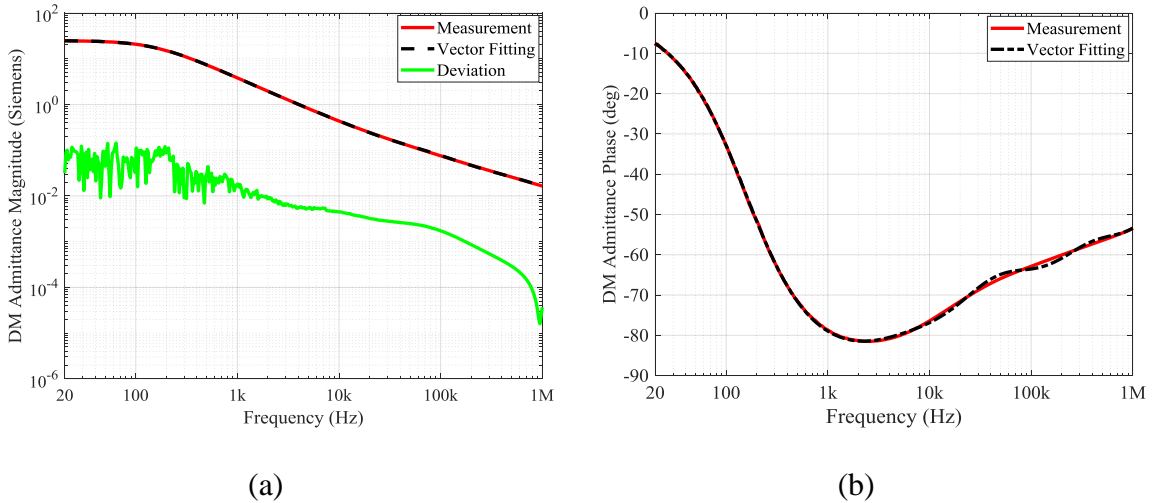


Figure 4. The demonstration of the good agreements between the vector fitting results and measurement data in the comparisons of: (a) DM admittance magnitude, (b) DM admittance phase. The deviations in (a) are in the range of 10^{-5} to 10^{-1} .

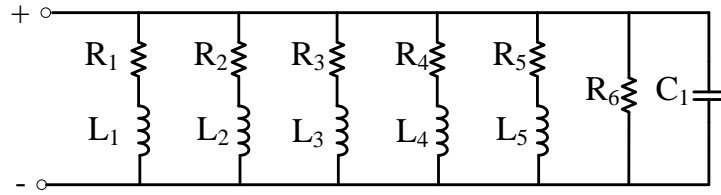


Figure 5. The generated one-port equivalent circuit model through the vector fitting method and based on the measured motor DM admittance.

Table 4. Component Values in the Circuit Model in Figure 5

Name	Value	Name	Value
R_1	$79.5515 \, \Omega$	L_1	$21.059 \, \mu H$
R_2	$19.7531 \, \Omega$	L_2	$47.598 \, \mu H$
R_3	$12.7863 \, \Omega$	L_3	$295.98 \, \mu H$
R_4	$0.0448 \, \Omega$	L_4	$44.813 \, \mu H$
R_5	$0.3642 \, \Omega$	L_5	$606.92 \, \mu H$
R_6	$161.2903 \, \Omega$	C_1	$12.369 \, pF$

As seen from Figure 6, the motor CM impedance exhibits a capacitive behavior in the low frequency band. Therefore, the equivalent circuit model illustrated in Figure 7 considering both motor DM and CM characteristics is developed by adding the equivalent capacitors between the three terminals abovementioned and the reference GND which is the fourth terminal in the circuit model. The physical meanings of C_u , C_v , and C_w are the parasitic capacitances between the stator coil and motor metal housing for each phase, and their values are determined with respect to the measured CM impedance magnitude and the circuit topology.

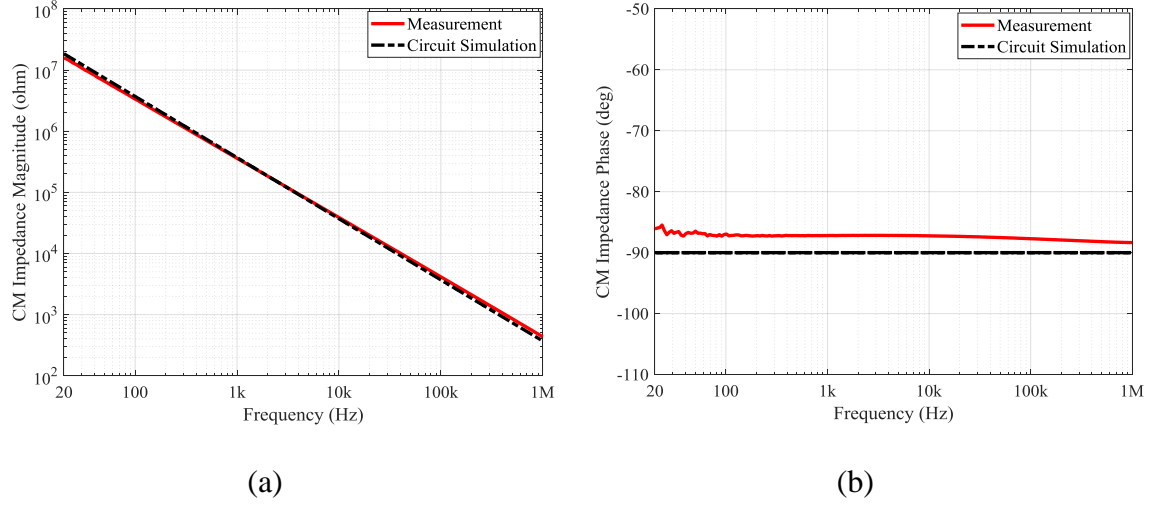


Figure 6. The comparisons between the simulation results obtained through the circuit model shown in Figure 7 and the measurement data: (a) CM impedance magnitude comparison, (b) CM impedance phase comparison.

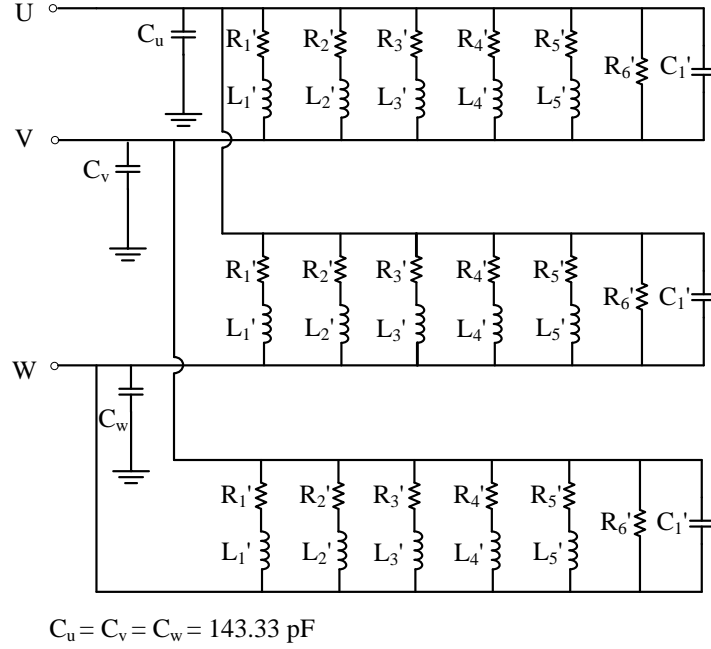


Figure 7. The equivalent circuit model considering both motor CM and DM characteristics in the low frequency band.

Since the ports can be defined between each phase terminal and the reference GND, the equivalent circuit model in Figure 7 is employed to create the S-parameter

matrix in the low frequency band. The data is extrapolated in the frequency range of DC to 20 Hz.

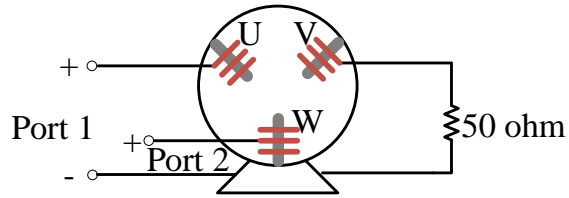


Figure 8. The representation of the arrangement at the motor terminals during the S-parameter measurements.

4. MOTOR MODELING IN THE HIGH FREQUENCY BAND

The S-parameter measurements are conducted using Agilent E5071C in the high frequency band. A representation of the arrangement at the PMSM terminals during the measurements is displayed in Figure 8. The $3 \times 3 \times N$ S- parameter matrix is assembled subsequently.

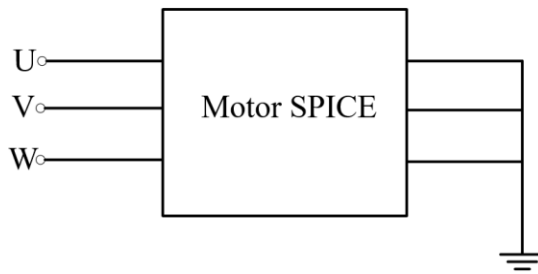


Figure 9. The generated motor SPICE model in the frequency range of DC to 120 MHz.

The S-parameter matrix in the entire frequency range of interest is formed by combining the two matrices in the low and high frequency ranges. The SPICE model

demonstrated in Figure 9 is generated in ANSYS environment where a vector fitting algorithm is applied and the tolerated fitting error is not exceeding 0.02%.

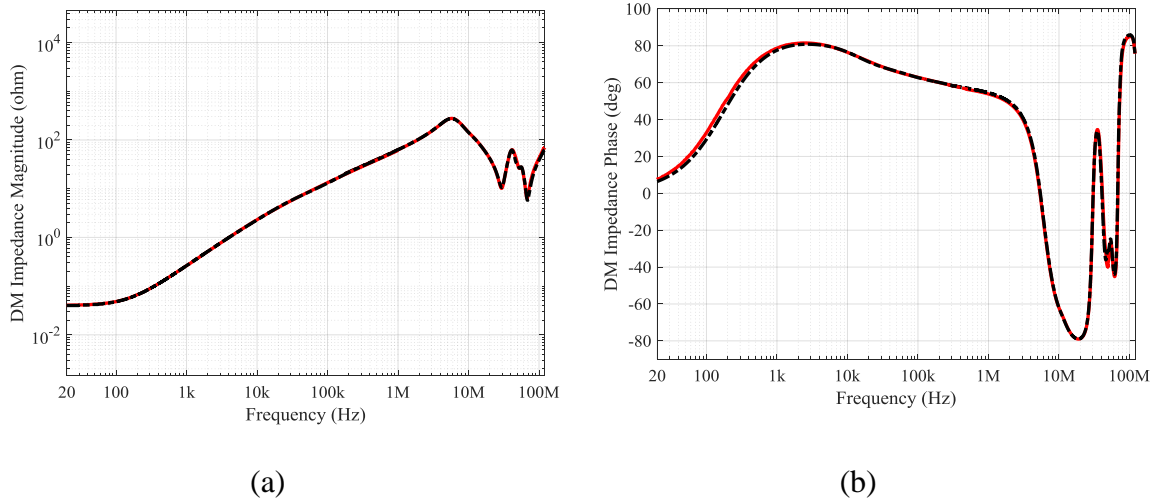


Figure 10. Verification of the constructed motor SPICE model through the comparison of motor DM impedance: (a) DM impedance magnitude, (b) DM impedance phase.

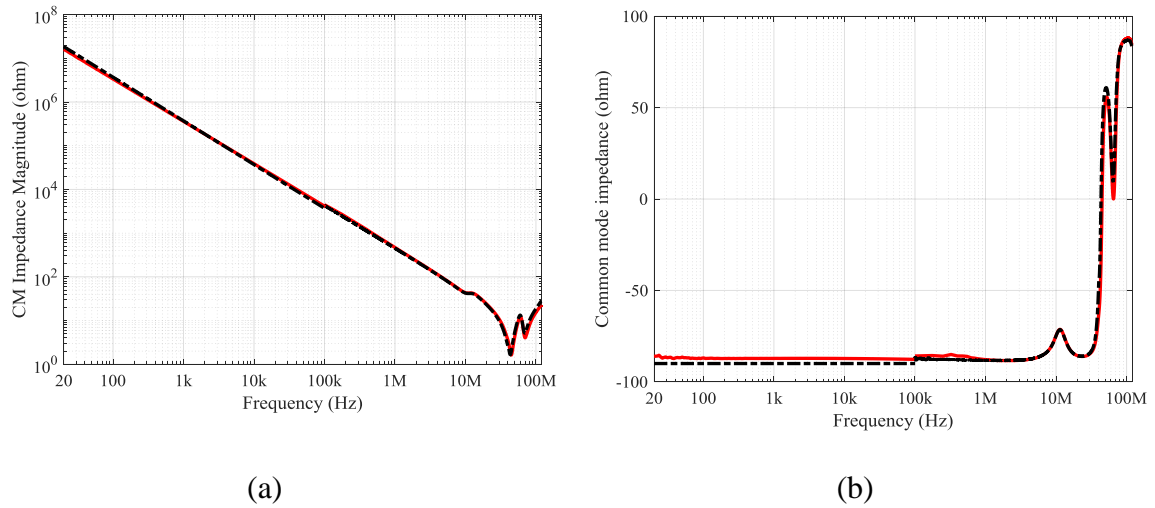


Figure 11. Verification of the constructed motor SPICE model through the comparison of motor CM impedance: (a) CM impedance magnitude, (b) CM impedance phase.

The verification of the developed motor SPICE model is performed throughout the comparisons of motor DM and CM impedances between the simulation and measurement results presented in Figure 10 and Figure 11, respectively.

5. CONCLUSION

The systematic, accurate and broadband modeling methodology based on the vector fitting approach for a typical PMSM utilized in the three-phase motor-drive braking system is presented in this paper. The simulated results using the proposed modeling methodology and measurement data is correlated. The created motor SPICE model is valid from DC up to 120 MHz, which is suitable for both frequency- and time-domain simulations. The proposed modeling method can be expanded as a generic EMI modeling technique for any three-phase motors.

REFERENCES

- [1] Y. Xiong, X. Li, Y. Li, and X. Zhao, "A high-frequency motor model constructed based on vector fitting method," in Proc. IEEE Int. Symp. EMC & AP EMC, Sapporo, Japan, 3-7 June, 2019.
- [2] CISPR 25: 2016, Vehicles, boats and internal combustion engines – Radio disturbance characteristics – Limits and methods of measurement for the protection of on-board receivers.
- [3] J. Lee, J. Ha, M. Kim, S. Yun, Y. Kim, and W. Nah, "Prediction of conducted emission in a PMSM-drive braking system using a circuit model combined with EM simulation," International Journal of Automotive Technology, vol. 20, no. 3, pp. 487-498, May 2019.

- [4] K. Gulez and A. A. Adam, "High-frequency common-mode modeling of permanent magnet synchronous motors," *IEEE Transactions on EMC*, vol. 50, no. 2, pp. 423-426, May 2008.
- [5] S. Yun, J. Ha, M. Kim, C. Lee, Y. Kim and J. Yoo, "Integrated modeling of a motor driven system for analysis of conducted emissions," in *Proc. Int. Symp. EMC - EMC Europe*, Wroclaw, Poland, 5-9 Sep. 2016.
- [6] J. Lee, M. Kim, J. Ha, C. Lee, S. Yun, Y. Kim, K. Nam and W. Nah, "Modeling of conducted EMI with current probe method for a motor-drive braking system," in *Proc. Int. Symp. EMC - EMC Europe*, Angers, France, 4-7 Sep. 2017.
- [7] J. Lee, J. Ha, M. Kim, C. Lee, S. Yun, Y. Kim and W. Nah, "System-level modeling of conducted emission in motor driving circuit for brake system," in *Proc. IEEE Int. Symp. EMC & APEMC*, Seoul, Korea, 20-23 June, 2017.
- [8] J. Xue, F. Wang and B. Guo, "EMI noise mode transformation due to propagation path unbalance in three-phase motor drive system and its implication to EMI filter design," in *Proc. IEEE Applied Power Electronics Conference and Exposition (APEC)*, Fort Worth, TX, USA, 16-20 Mar. 2014.
- [9] D. Bellan, "Mode transformation of EMI noise due to unbalanced filter capacitors in three-phase motor drive systems," *IECON 2017 – 43rd Annual Conference of the IEEE industrial Electronics Society*, Beijing, China, Oct. 29 - Nov. 1, 2017.
- [10] S. Wang and F. C. Lee, "Investigation of the transformation between differential-mode and common-mode noises in an EMI filter due to unbalance," *IEEE Transactions on EMC*, vol. 52, no. 3, pp. 578-587, Aug. 2010.
- [11] M. Kamikura, Y. Murata, and A. Nishizawa, "Investigation on the mode conversion between common-mode and differential-mode noises in EMI filters for power electronics circuits," in *Proc. Int. Symp. EMC*, Brugge, Belgium, 2-6 Sep. 2013.
- [12] Y. Guo, S. Penugonda, M. Kim, J. Lee, J. Ha, S. Yun, J. Fan, and H. Kim, "Ground bridge effect on reduction of conducted emission from three-phase motor drive system," in *Proc. Int. Symp. EMC - EMC Europe*, Barcelona, Spain, 2-6 Sep. 2019.
- [13] A. Consoli and G. Oriti, "Induction motor modeling for common mode and differential mode emission evaluation," in *Conf. Rec. IEEE IAS Annu. Meeting*, San Diego, CA, USA, 7-11 Oct. 1996.
- [14] A. Boglietti and E. Carpaneto, "Induction motor high frequency model," in *Conf. Rec. 34th IEEE IAS Annu. Meeting*, vol. 3, pp. 1551-1558, 1999.

- [15] M. Schinkel, S. Weber, S. Guttowski, W. John, and H. Reichl, "Efficient HF modeling and model parameterization of induction machines for time and frequency domain simulation," in Proc. Twenty-First Annual IEEE Applied Power Electronics Conference and Exposition, Dallas, TX, USA, 19-23 Mar. 2006.
- [16] B. Revol, J. Roudet, J. L. Schanen, and P. Loizelet, "EMI study of three-phase inverter-fed motor drives," IEEE Transactions on Industry Applications, vol. 47, no. 1, pp. 223-231, Jan./Feb. 2011.
- [17] L. Yang, S. Wang, and J. Feng, "Electromagnetic interference modeling and suppression techniques in variable-frequency drive systems," Frontiers of Mechanical Engineering, pp. 329-353, Nov. 2017.
- [18] B. Gustavsen and A. Semlyen, "Rational approximation of frequency domain responses by vector fitting," IEEE Transactions on Power Delivery, vol. 14, no. 3, pp. 1052-1061, Jul. 1999.
- [19] B. Gustavsen, "Improving the pole relocating properties of vector fitting," IEEE Transactions on Power Delivery, vol. 21, no. 3, pp. 1587-1592, Jul. 2006.
- [20] L. Li, W. He, Y. Wang, and X. Li, "Modeling of the wide frequency equivalent circuit of the three-phase AC motor based on vector fitting method," Int. J. Electric and Hybrid Vehicles, vol. 11, no. 1, pp. 12-22, Mar. 2019.
- [21] Q. Wang, F. Zhang, H. Peng, Q. Liu, and X. Li, "Permanent magnet synchronous AC motor EMI model based on vector-fitting," Transactions of China Electrotechnical Society, vol. 30, Mar. 2015.
- [22] G. Antonini, "SPICE equivalent circuits of frequency-domain responses," IEEE Transactions on EMC, vol. 45, no. 3, pp. 502-512, Aug. 2003.
- [23] M. Moreau, N. Idir, and P. L. Moigne, "Modeling of conducted EMI in adjustable speed drives," IEEE Transactions on EMC, vol. 51, no. 3, pp. 665-672, Aug. 2009.

II. TIME-EFFICIENT WORST-CASE GLASS-WEAVE SKEW ESTIMATION FOR MICROSTRIP-LINES

Y. Guo

Department of Electrical Engineering, Missouri University of Science and Technology,
Rolla, MO 65409

Email: ydggdd@umsystem.edu

ABSTRACT

Glass-weave skew (GWS), resulting from varying dielectric constant (D_k) around the signal trace, is dominant source of total line-to-line skew in differential signaling. The relative locations between signal conductors and glass fibers are random in real printed circuit boards (PCBs), which introduces significant uncertainty in the resulting GWS. Thus, it is desired to develop a feasible methodology for worst-case GWS prediction, so that engineers can evaluate their high-speed designs. However, due to the statistical characteristic of GWS problems and complexity involved in the inhomogeneous dielectric, predicting the worst-case scenario is regarded as a challenging task. The traditional GWS evaluation methods require either full-wave simulations or measurements of numerous test vehicles, which is time-consuming. Herein, a time-efficient approach for worst-case estimation of GWS is presented and applicable to microstrip-lines. Using the divide-and-conquer strategy, only cross-sectional geometries, trace-rotation angle, and dimensions of glass fibers are necessary for the calculations. A statistical approach is employed to determine the local D_k values of each segment through analytical expressions, which can capture and accommodate to the material inhomogeneity. Good correlation is reached between the predicted data and baseline

results, and it takes less than twenty seconds to finalize the GWS estimation in the MATLAB-based environment.

Keywords: dielectric constant (Dk), differential signaling, divide and conquer, glass-weave skew (GWS), intra-pair skew, material inhomogeneity

1. INTRODUCTION

Differential signaling has been widely employed in high-speed interconnect design due to its superior noise rejection and cancellation. However, the induced timing skew by various factors between positive and negative signal conductors may introduce excessive crosstalk [1] and deterministic jitter [2], which could undermine the signal integrity of a high-speed channel built on a printed circuit board (PCB). In addition, the difference in propagation velocities between the two traces in a differential pair may lead to a common mode voltage and a further degraded differential signal [3]. Only a few picoseconds of skew could be problematic when data rate is beyond 28 giga bit per second [4].

It is well-known that the skew induced by glass weave effect is a dominating source of total skew for differential pairs running on PCBs. The major components in PCB dielectrics are glass fiber and epoxy-resin, which introduces an inhomogeneous medium. According to the current technology, the relative dielectric constant (Dk) of a glass fiber is generally about 1.5-to-2.4 times larger than that of a typical resin [5]. Therefore, the effective local Dk values seen by the two coupled traces could be different and location-dependent along the propagation direction, which may result in glass-weave

skew (GWS). There is another product of glass weave effect, namely, the periodic loading. It may produce extra insertion loss at the resonance frequency which is governed by the pitch size of two neighboring glass bundles [6].

One common practice to mitigate GWS is the usage of a rotation angle between trace and weaving fibers [6]. However, the alignment of signal lines to glass weave in a real PCB is random during manufacturing process, and the resulting GWS could vary for a given glass weave rotation angle or an equivalent trace rotation angle. Therefore, it necessitates the estimation of the maximum, or in other words, the worst-case GWS, for a given design. Besides, the maximum tolerated intra-pair skew for most high-speed serial links have been specified in datasheets [7], and the budget could shrink with the ever-increasing data rates.

Traditionally, predicting GWS could be difficult and time-consuming, considering the complex composited PCB material comprising of inhomogeneous dielectric layers and the inherent statistical nature of GWS problems. It may require full-wave simulation-based analysis [2], [8], [9], or the study based on massive experiments performed on various test vehicles [3], [4], [7], [11], or the involvement of both full-wave simulations and real measurements [6], [10]. An attempt to predict and analyze the distribution of GWS through a 2D finite element method based electromagnetic (EM) solver is illustrated in [12], where the microstrip-lines are in parallel with the glass fiber in the warp direction but perpendicular in weft direction. However, this is not a good representative of the routing in real world and in consequence oversimplifies the problem.

An artificial neural network (ANN) is trained in [13] to explore the potential of utilizing a machine-learning algorithm for GWS prediction. The data points employed for

training are from full-wave simulations where the glass fibers are placed orthogonally to signal traces in the weft direction. Although the good agreement between full-wave simulation results and ANN predicted data is reached, it should be noted that the proposed ANN is dedicated to the predefined glass types, PCB materials, and cross-sectional geometries of the differential striplines in the study. When any of these parameters change, the ANN must be updated, which demands a laborious process where multiple full-wave simulations are involved. Furthermore, the model in [13] is not able to provide insights onto the physics of a GWS problem.

Since worst-case glass weave skew estimation is desired, the emphasis of this study is placed on the development of a time-efficient methodology for worst-case GWS prediction, which can be integrated in the early design stage of a high-speed serial link. The information of cross-sectional parameters, trace-rotation angle, glass fiber's geometries and electrical properties, and resin dielectric constant can be readily obtained from design files or PCB vendors. Thus, they are treated as known inputs in the study.

The overall modeling strategy and the analysis of coupling terms' influence on GWS are presented first, followed by the determination of local D_k values through analytical formulas. The proposed method is applied to the full-wave simulation-based studies, which verify the robustness and feasibility of the algorithm. It is found that the GWS estimation takes less than twenty seconds for a given structure in a MATLAB environment.

2. MODELING STRATEGY

2.1. OVERALL MODELING STRATEGY: DIVIDE AND CONQUER

To reduce the geometry complexity, the divide-and-conquer strategy is adopted. Assuming a pair of coupled differential microstrip-lines whose top view is illustrated in Figure 1 (a), the glass fibers are modeled as the orthogonal rectangles. The resin is omitted in the figure for the sake of clarity, yet it is included in the model under study.

Through segmentation, each signal conductor can be divided into several segments which fall into two categories. In the first category, the material underneath signal conductor is either glass fiber or a composite of glass and resin (see segments i and j in Figure 1(a)). However, it would become pure resin for the segments of second category (see segment k in Figure 1(a)). To be more precise, the materials of segments i and j are both mixtures of glass fiber and resin. This material inhomogeneity is addressed in the determination of local D_k values, where a statistical approach is employed.

The total propagation delay of one line is regarded as the summation of delays of every fraction. Therefore, the problem of estimating total GWS can be simplified, if the delay of each segment can be determined.

2.2. THE INFLUENCE OF COUPLING TERMS ON GWS

From the crosstalk point of view, the coupling noise from the aggressor can influence the waveform transmitted on the victim line, resulting in the change in transition delay [14]. The impact of coupling terms on GWS is evaluated through a full-wave simulation-based analysis.

Starting from the modified mixed-mode S-parameters in (1) [15], where, the incident power are classified into differential-mode (a_{dm1}, a_{dm2}) and common-mode (a_{cm1}, a_{cm2}) waves, and the reflected waves at each port (b_1, b_2, b_3, b_4) are acquired through the elements S_{idj} and S_{icj} , which denote the relationship between the reflected and differential-mode incident waves, and relationship between reflected and common-mode incident waves, respectively.

$$\begin{pmatrix} b_1 \\ b_2 \\ b_3 \\ b_4 \end{pmatrix} = \begin{pmatrix} S_{1d1} & S_{1d2} & S_{1c1} & S_{1c2} \\ S_{2d1} & S_{2d2} & S_{2c1} & S_{2c2} \\ S_{3d1} & S_{3d2} & S_{3c1} & S_{3c2} \\ S_{4d1} & S_{4d2} & S_{4c1} & S_{4c2} \end{pmatrix} \begin{pmatrix} a_{dm1} \\ a_{dm2} \\ a_{cm1} \\ a_{cm2} \end{pmatrix} \quad (1)$$

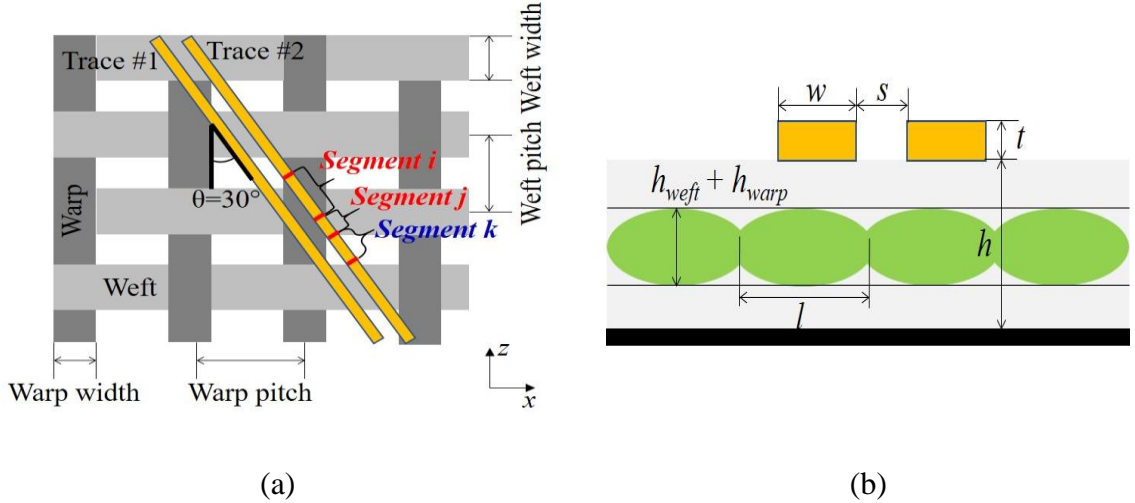


Figure 1. Illustration of the differential microstrip-line under study: (a) the top view and demonstration of trace segmentation, (b) a simplified cross-section showing the definitions of geometrical parameters.

Table 1. Values of Geometrical Parameters

Parameter	Value	Parameter	Value
h_{weft}	1.5 mil	w	4.0 mil
h_{warp}	1.9 mil	s	3.0 ~ 10.0 mil
h	6.0 mil	t	1.2 mil

Assuming odd-even port order, the intra-pair skew is determined by the difference in the phase velocities of each trace (v_{p1}, v_{p2}) [15], using

$$e^{-\gamma_1 l_1} = \left\{ \frac{1 - S_{1d1}^2 + S_{2d1}^2}{2S_{2d1}} \pm A_1 \right\}^{-1}. \quad (2)$$

$$A_1 = \sqrt{\frac{(S_{1d1}^2 - S_{2d1}^2 + 1)^2 - (2S_{1d1})^2}{(2S_{2d1})^2}}. \quad (3)$$

$$\beta_1 = \text{imag}(\gamma_1), v_{p1} = \frac{\omega}{\beta_1}. \quad (4)$$

$$e^{-\gamma_2 l_2} = \left\{ \frac{1 - S_{3d1}^2 + S_{4d1}^2}{2S_{4d1}} \pm A_2 \right\}^{-1}. \quad (5)$$

$$A_2 = \sqrt{\frac{(S_{3d1}^2 - S_{4d1}^2 + 1)^2 - (2S_{3d1})^2}{(2S_{4d1})^2}}. \quad (6)$$

$$\beta_2 = \text{imag}(\gamma_2), v_{p2} = \frac{\omega}{\beta_2}. \quad (7)$$

It is noted that the two coupling terms representing far-end crosstalk (FEXT), namely, S_{23} and S_{41} , are incorporated in the calculations since [15], [16]

$$S_{2d1} = \frac{1}{\sqrt{2}}(S_{dd21} + S_{cd21}) = \frac{1}{\sqrt{2}}(S_{21} - S_{23}). \quad (8)$$

$$S_{4d1} = \frac{1}{\sqrt{2}}(S_{dd21} - S_{cd21}) = \frac{1}{\sqrt{2}}(S_{43} - S_{41}). \quad (9)$$

For the microstrip-line under study, the definitions and values of cross-sectional geometries are shown in Figure 1 (b) and Table 1, correspondingly. The impact of FEXT on GWS is evaluated through the full-wave simulation-based comparison exhibited in Figure 2 (a), where the results with coupling terms accounted are treated as the baseline.

The width of glass fiber l is dependent on both the nominal values and trace rotation angle, and the width is 14.1 mil in the simulations. The trace spacing s is swept from 3.0 mil to 10.0 mil with 1.0 mil step size, to mimic the transition from tightly to loosely coupling scenarios. The Dk values of glass fiber and resin are chosen to be 6.6 (the typical value for E-glass) and 3.0 (the typical value of most epoxy-resin) at 1 GHz, respectively. The loss tangent (Df) of the two materials is set to be identical for the sake of problem simplification, since Df does not affect phase velocity, and the value is 0.006 at 1 GHz. The physical length of the coupled differential pair is assumed to be 500 mil. In fact, the length of one segment in Figure 1 (a) is much smaller compared against this value, given that the length of a general glass bundle and the associated pitch size are usually less than 25 mil [17]. Therefore, it is regarded as an extreme case for the evaluation. The simulations are conducted in ANSYS HFSS.

The close agreement in Figure 2 (a) implies that the coupling terms have negligible impact on the GWS of the simulated differential pair, due to the fact that the magnitude of FEXT is at least about 20 dB lower than that of insertion loss in the frequency range of interest, which is suggested in Figure 2 (b).

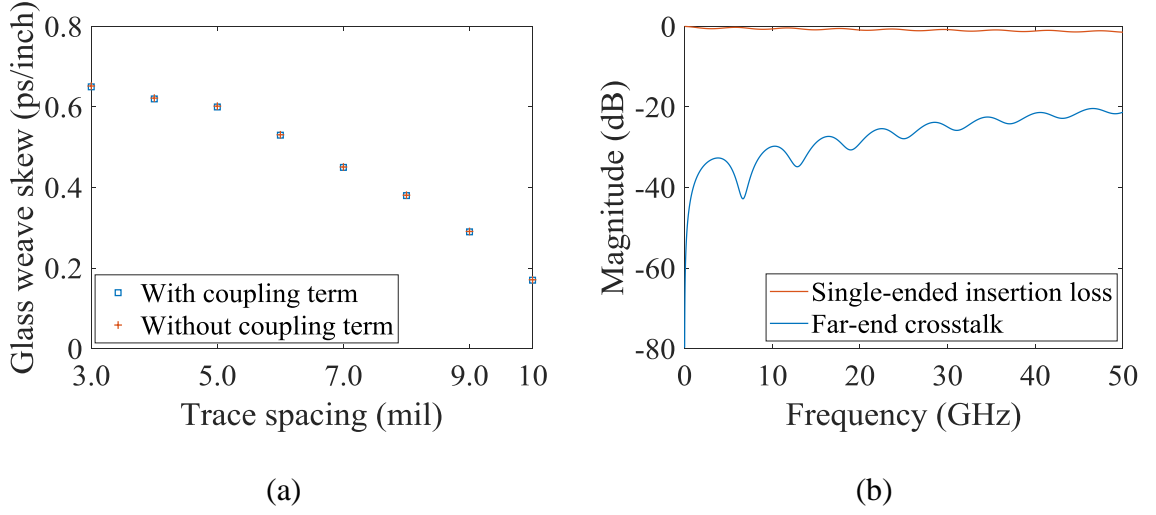


Figure 2. Full-wave simulation-based study: (a) comparison of calculated GWS to reveal the impact of coupling terms, (b) comparison of insertion loss and FEXT magnitudes, which indicates that the coupling terms can be ignored in GWS calculations.

Since FEXT magnitude is generally proportional to the length of differential line, and insertion loss tends to be smaller for the traces with shorter length, it is concluded that it is safe to ignore the coupling terms in the GWS calculation for one little fraction of the differential pair in Figure 1 (a). Thus, the transition delay of each signal line can be deduced separately.

3. DETERMINATION OF LOCAL DK VALUES

Assuming a single-ended microstrip-line, its cross-section is illustrated in Figure 3 (a). Under statistical condition, the associated electric potential $\phi(x, y)$ is governed by the Poisson's equation [18]:

$$\frac{\partial^2 \phi(x, y)}{\partial y^2} = -\frac{\rho(x, y)}{\epsilon}. \quad (10)$$

The general solution of Poisson's equation is a liner combination of $e^{\beta y}$ and $e^{-\beta y}$ [19].

Solving for the unique solution to the second-order partial differential equation in (6) requires the boundary and continuity conditions in (11), where $\rho(\beta)$ denotes the distribution of electric charge density after Fourier transformation, and ϵ_0 is the permittivity of air.

$$\phi_1(\beta, y)|_{y=0} = 0. \quad (11a)$$

$$\phi_1(\beta, y)|_{y=a} = \phi_2(\beta, y)|_{y=a}. \quad (11b)$$

$$\epsilon_1 \frac{\partial \phi_1(\beta, y)}{\partial y} \Big|_{y=a} = \epsilon_2 \frac{\partial \phi_2(\beta, y)}{\partial y} \Big|_{y=a}. \quad (11c)$$

$$\phi_2(\beta, y)|_{y=a+b} = \phi_3(\beta, y)|_{y=a+b}. \quad (11d)$$

$$\epsilon_2 \frac{\partial \phi_2(\beta, y)}{\partial y} \Big|_{y=a+b} = \epsilon_3 \frac{\partial \phi_3(\beta, y)}{\partial y} \Big|_{y=a+b}. \quad (11e)$$

$$\phi_3(\beta, y)|_{y=a+b+c} = \phi_4(\beta, y)|_{y=a+b+c}. \quad (11f)$$

$$\epsilon_3 \frac{\partial \phi_3(\beta, y)}{\partial y} \Big|_{y=a+b+c} = \epsilon_4 \frac{\partial \phi_4(\beta, y)}{\partial y} \Big|_{y=a+b+c} + \frac{\rho(\beta)}{\epsilon_0}. \quad (11g)$$

$$\phi_4(\beta, y)|_{y=\infty} = 0. \quad (11h)$$

The statistical line capacitance yields

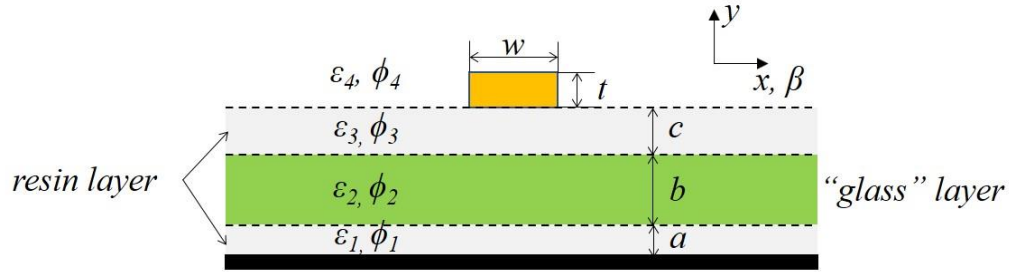
$$\frac{1}{C_{inhomo}} = \frac{1}{2\pi Q^2} \int_{-\infty}^{\infty} \rho(\beta) \phi(\beta, a + b + c) h(\beta) d\beta. \quad (12)$$

$$h(\beta) = 0.5 \left[1 + \frac{\sinh(|\beta|d - |\beta|t)}{\sinh(|\beta|d)} \right]. \quad (13)$$

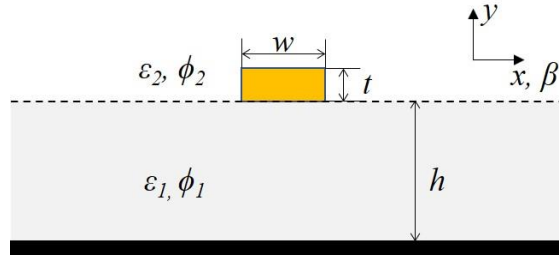
The line capacitance is proportional to the effective Dk value of inhomogeneous material. With all the dielectrics replaced by air, the effective Dk can be computed through

$$Dk_{eff} = \frac{C_{inhomo}}{C_{air}}. \quad (14)$$

The derived general expressions of C_{inhomo} for the cross-section given in Figure 3 (a) are shown in the Appendix.



(a)



(b)

Figure 3. Cross-sections that are used for determination of local Dk values: (a) for the segments in the first category (segments i and j in Figure 1 (a)), (b) for the segments in the second category (segment k in Figure 1 (a)).

For the segments i and j in Figure 1 (a), which belong to the first category, their cross-sections can be represented using Figure 3 (a), in which a “glass layer” is defined and bounded by the height of a glass bundle. A portion of resin is integrated into the “glass layer”, which necessitates the estimation of effective Dk value for this composite.

The Hashin-Shtrikman mixing rule [19] is adopted for the determination of ε_2 in Figure 3 (a), which yields

$$\varepsilon_2 = V_{glass}\% \times Dk_{glass} + V_{resin}\% \times Dk_{resin}. \quad (15)$$

where, V_{glass} and V_{resin} are the volume ratios of glass fiber and resin for one segment, respectively. They can be decided by the resin content percent, the geometries, and density information.

The cross-section of the segments in the second category, e.g., segment k in Figure 1 (a), is sketched in Figure 3 (b). The governing equation is still valid herein. However, less boundary and continuity conditions are needed for solving for the unique solution, since there are only two dielectric layers in this case.

The underlying critical assumption is that, it is assumed the effective local Dk values are deduced only by the materials directly below the signal conductors. However, according to Hashin-Shtrikman mixing rule, the exact local Dk values of segments i and j may be a little bit smaller than the values evaluated through the aforementioned method, since there are epoxy-resin adjacent to the edges of these segments along the trace direction, and epoxy-resin usually has a smaller Dk value. Contrastingly, the accurate local Dk value of segment k would be larger than the estimated result. Therefore, the hypothesis is only feasible for transition delay estimation, since the errors in these two categories could be cancelled by symmetricity.

The transition delay of one segment, with physical length l_{length} , is computed through (11) where c is the light speed in free space. Adding up the delays of every segment gives the total transition delay of one signal line. The GWS can be readily determined afterwards.

$$T_{delay} = \frac{l_{segment} \times \sqrt{Dk_{eff}}}{c}. \quad (16)$$

4. VALIDATIONS AND DISCUSSION

The proposed algorithm is verified through full-wave simulation-based studies. The cross-sectional coefficients in Table 1 are adopted, except that the trace spacing, s , is fixed and equals to 5 *mil*. The Dk values of a typical E-type 3313 glass (equals to 6.6 at 1 GHz according to datasheet) and epoxy-resin (equals to 3.0 at 1 GHz) are assigned to the dielectrics, whose loss tangents are 0.006 at 1 GHz. For 3313 glass, the warp and weft widths are 13.1 *mil* and 11.0 *mil*, respectively, and the warp pitch and weft pitch sizes are 16.2 *mil* and 16.3 *mil* sequentially [17]. The entire length of the microstrip-line under study is 8 *inches*.

Two different cases are designed in order to validate the GWS prediction methodology. All simulations are facilitated in ANSYS HFSS.

4.1. COMPARISON OF GWS WITH DIFFERENT TRACE LOCATIONS

In the first case, the relative location of signal conductors to weaving glass is manipulated in the full-wave simulations, while trace-rotation angle is maintained to be 30 degree, mimicking the random alignment of differential traces to glass weave which could happen in the high-volume production phase. The trace locations are swept from left to right, as indicated in Figure 4, and the sweeping step is 1 *mil*.

The baseline data of GWS are acquired through the equations (2) and (3), where the simulated S-parameters are involved in the calculations. The results obtained using

the proposed approach are compared with the baseline, and good correlation has been achieved, as suggested in Figure 5. It is found that the worst-case GWS happens when the trace location is near either the start or end point, and the value is about -14 ps. The transition delay of Trace #1 is subtracted by that of Trace #2 in Figure 4, resulting the negative values for the calculated GWS in Figure 5.

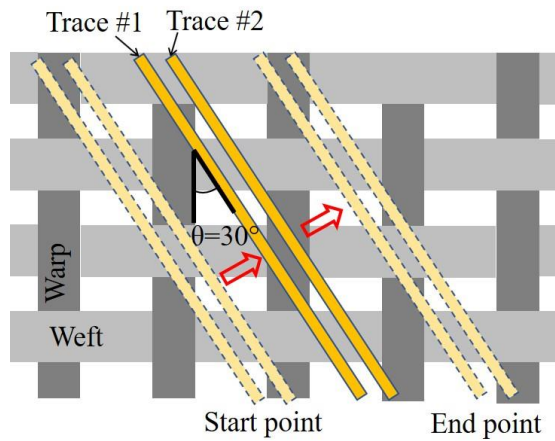


Figure 4. Top-view sketch of the microstrip-lines in the full-wave simulations and demonstration of how trace location is swept with the illustrations of start point, end point, and sweeping direction.

4.2. COMPARISON OF GWS WITH DIFFERENT TRACE ROTATION ANGLE

The measurement-based studies presented in [3] reveal that there exists a trace-rotation angle for GWS mitigation, at which GWS can reach its minimum value. This magic angle is around 10 degree according to [3]. The trace-rotation angle is changed from 0 to 45 degree in the second case with 5-degree step, in order to manifest this conclusion.

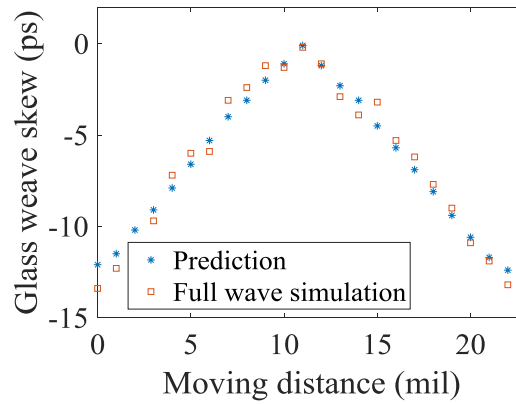


Figure 5. Comparison of GWS when manipulating signal trace locations. Good correlation is achieved.

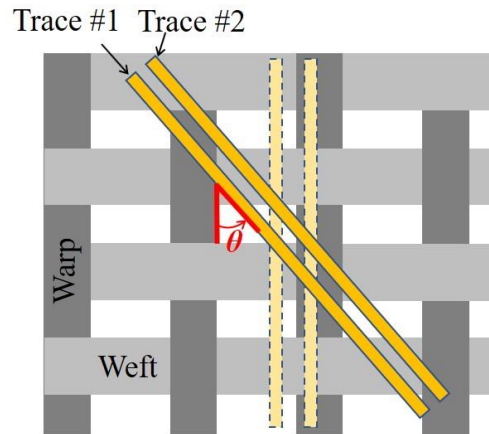


Figure 6. Illustration of how trace-rotation angle is changed through the top view of the microstrip-lines in the simulations.

The trace rotation direction is described in Figure 6. Again, the GWS data calculated based upon the full-wave simulation results are treated as baseline, and they are compared against the outputs when using the algorithm proposed in this paper. It is evident that close agreement is reached, as implied in Figure 7. The GWS has its maximum value, around -22 ps, when the trace-rotation angle is zero degree, and the

magnitude decreases to the minimal, approximately -1.8 ps, at 10-degree rotation angle.

This conclusion reflects the observations in [3].

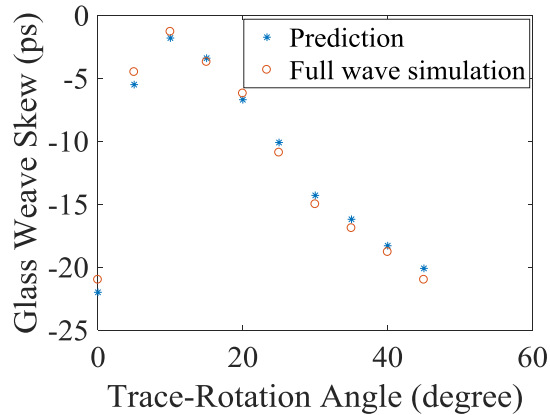


Figure 7. Comparison of GWS when manipulating signal-rotation angle. Good agreement is reached.

Table 2. Server Hardware Settings

Processor	Intel [®] Xeon [®] Gold 6136 CPU @ 3.00 GHz 2.99 GHz (2 processors)
RAM	512 GB available
System Type	64-bit operating system

4.3. COMPARISON OF TIME CONSUMPTIONS

A high-performance server is employed for the full-wave simulations, and the GWS calculations are carried out in a MATLAB-based environment on a laptop. Table 2 details the hardware settings of the server.

Table 3. Comparison of Time Consumption

	One Single Full-Wave Simulation	The Developed Method
Time Consumption	6 h 55 min 32 s	19.1 s

The comparison of time consumption is given in Table 3. It is found that one single full-wave simulation takes as long as around 7 hours. By contrast, the computation time is less than 20 s if using the developed methodology.

4.4. DISCUSSION

The maximum error between the predicted GWS results and baseline is less than 8% in the validations, which is generally good in the early design stage.

The main errors may be introduced by the hypothesis involved in the cross-sections used for local D_k determination. The simplification in (10) may bring in a portion of errors as well.

5. CONCLUSION

Due to the inhomogeneous material and complex structures of glass weave, prediction of GWS can be quite challenging and time-consuming. A methodology for the time-efficient worst-case GWS estimation is presented and validated in this paper. The divide-and-conquer strategy is adopted in the algorithm to simplify the GWS prediction problem. A statistical approach is used to determine the local D_k values. Excellent

agreement between the predicted data and baseline results have been obtained. The proposed method can be integrated into high-speed interconnect design.

APPENDIX

The general expression of C_{inhomo} is given in A (1).

$$C_{inhomo} = \frac{2\pi}{\int_{-\infty}^{\infty} K_1 \cdot [M_1 \sinh(\beta c) + M_2 \cosh(\beta c)] d\beta}. \quad A(1)$$

The expressions of K_1 , M_1 and M_2 yield

$$K_1 = \left[\frac{2\sin(\frac{\beta w}{2})}{\frac{\beta w}{2}} - \left(\frac{\sin(\frac{\beta w}{4})}{\frac{\beta w}{4}} \right)^2 \right]^2 \cdot h(\beta). \quad A(2)$$

$$M_1 = \frac{\varepsilon_1}{\varepsilon_3} \cosh(\beta b) \cosh(\beta a) + \frac{\varepsilon_2}{\varepsilon_3} \sinh(\beta b) \sinh(\beta a). \quad A(3)$$

$$M_2 = \frac{\varepsilon_1}{\varepsilon_2} \cosh(\beta a) \sinh(\beta b) + \sinh(\beta a) \cosh(\beta b). \quad A(4)$$

REFERENCES

- [1] Ahmet C. Durgun and Kemal Aygün, “Fiber weave impact on crosstalk of high speed communication channels in glass epoxy packages,” in Proc. IEEE Int. Symp. Electromagn. Compat., Jul. 25-29, 2016, pp. 35-39.
- [2] Yuriy Shlepnev and Chudy Nwachukwu, “Modelling jitter induced by fibre weave effect in PCB dielectrics,” in Proc. IEEE Int. Symp. Electromagn. Compat., Aug. 4-8, 2014, pp. 803-808.
- [3] Jeff Loyer, Richard Kunze, and Xiaoning Ye, “Fiber weave effect: practical impact analysis and mitigation strategies,” in Proc. DesignCon, 2007, pp. 1-28.

- [4] M. J. Degerstrom, and et al., "System level approach for assessing and mitigating differential skew for 10+ Gbps SerDes applications," in Proc. IEEE 58th Elec. Comp. and Tech. Conf., May 27-30, 2008, pp. 513-520.
- [5] Michael. J. Gay and Richard Pangier, "Making sense of laminate dielectric properties," in Proc. Int. Symp. Microelectronics, Fall 2011, pp. 000293-000301.
- [6] Kartheek Nalla, "Mitigation of glass weave skew using a combination of low Dk spread glass, multi-ply dielectric and routing direction," M.S. thesis, Elec. Eng. Dept., Missouri S&T, Rolla, MO, USA, 2016.
- [7] Eric Bogatin, Bill Hargin, Venkata Paladugu, Don DeGroot, Amendra Koul, Seungyong Baek, and Mike Sapozhnikov, "New characterization technique for class-weave skew," in Proc. DesignCon, 2017, pp. 1-27.
- [8] Xinxin Tian, Yao-Jiang Zhang, Jane Lim, Kelvin Qiu, Rick Brooks, Ji Zhang, and Jun Fan, "Numerical investigation of glass-weave effects on high-speed interconnects in printed circuit board," in Proc. IEEE Int. Symp. Electromagn. Compat., Aug. 4-8, 2014, pp. 475-479.
- [9] Surender Singh and Taranjit Kukal, "Timing skew enabler induced by fiber weave effect in high speed HDMI channel by angle routing technique in 3DFEM," in Proc. Elec.Perf. Elec. Pack. Syst. (EPEPS), Oct. 25-28, 2015, pp. 163-166.
- [10] Kartheek Nalla, Amendra Koul, Seungyong Baek, Mike Sapozhnikov, Giorgi Maghlakelidze, and Jun Fan, "Measurement and correlation-based methodology for estimating worst-case skew due to glass weave effect," in Proc. IEEE Int. Symp. Electromagn. Compat., Aug. 7-11, 2017, pp. 187-192.
- [11] Chris Herrick, Thomas Buck, and Ruihua Ding, "Bounding the effect of glass weave through simulation," in Proc. DesignCon, 2009, pp. 1-16.
- [12] Tong Zhang, "Statistical analysis of the fiber weave effect over differential microstrips on printed circuit boards," B.S. thesis, Undergrad. College, University of Illinois at Urbana-Champaign, Urbana, Illinois, 2014.
- [13] Jose Hejase, Pavel Paladhi, Roger Krabbenhoft, Zhaoqing Chen, Junyan Tang, and Dylan Boday, "A neural network based method for predicting PCB glass weave induced skew," in Proc. Elec.Perf. Elec. Pack. Syst. (EPEPS), Oct. 23-26, 2016, pp. 151-154.
- [14] Chung-Kuan Tsai and Malgorzata Marek-Sadowska, "Modeling crosstalk induced delay," in Proc. Fourth Int. Symp. Quality Elec. Design, Mar. 24-26, 2003.
- [15] Seungyong Baek, Eric Lee, and Baegin Sung, "Computation of intra-pair skew for imbalance differential line using modified mixed-mode S-parameter," in Proc. IEEE Elec. Perf. of Elec. Pack., Oct. 29-31, 2007, pp. 179-182.

- [16] Stephen. H. Hall and Howard. L. Heck, Advanced Signal Integrity for High-Speed Digital Designs. Hoboken, NJ, USA: Wiley, 2009.
- [17] Understanding Glass Fabric, Isola application note. Available at: <https://www.isola-group.com/resource/understanding-glass-fabric/>.
- [18] Eikichi Yamashita, "Variational method for the analysis of microstrip lines," IEEE Trans. on Microw. Theory Techn., vol. 16, no. 4, pp. 251-256, Apr. 1968.
- [19] Stanley J. Farlow, Partial Differential Equations for Scientists and Engineers, Dover Publications, Reprint edition, 1993.
- [20] Z. Hashin and S. Shtrikman, "A variational approach to the theory of the effective magnetic permeability of multiphase materials," Journal of App. Phy., vol. 33, pp. 3125-3131, 1962.

III. A COMPREHENSIVE STUDY ABOUT INHOMOGENEOUS DIELECTRIC LAYERS (IDLS) AND THE IMPACTS ON FAR-END CROSSTALK OF HIGH-SPEED PCB STRIPLINES

Y. Guo

Department of Electrical Engineering, Missouri University of Science and Technology,
Rolla, MO 65409

Email: ydggdd@umsystem.edu

ABSTRACT

Far-end crosstalk (FEXT) in typical high-speed PCB striplines is primarily attributed to dielectric inhomogeneity. In this paper, the inhomogeneity problem is comprehensively addressed by a novel algorithm that characterizes the dielectric constants (Dk s) of glass fibers and epoxy resin. In contrast to other methods, the proposed approach enables one to assess the impact of geometrical parameters on stripline FEXT and to estimate Dk_{core} and $Dk_{prepreg}$ based on Dk_{glass} and Dk_{resin} values extracted through analytical expressions. Full-wave simulations and real-board measurements are conducted to verify the proposed approach.

Keywords: far-end Crosstalk (FEXT), stripline, dielectric material, transmission-line theory.

1. INTRODUCTION

It is textbook knowledge that the magnitude of far-end crosstalk (FEXT) noise is zero for coupled striplines in printed circuit boards (PCBs) if the signal traces are

embedded in an ideal homogeneous medium [1]. However, there is an unavoidable need to use inhomogeneous dielectrics consisting of woven glass and epoxy resin with different dielectric constants (Dk s) for fabricating high-speed PCB striplines [2], which may result in observable FEXT, influencing the eye opening and introducing excessive timing jitter [3]-[5].

The components contributing to FEXT in striplines are examined and summarized in [4], where material inhomogeneity is identified as the dominant factor when the coupled signal traces are terminated with matched loads. The modal-based analysis [6]-[9] has revealed that the root cause of induced FEXT is the difference in the propagation delay between odd- and even-modes transmitted in an inhomogeneous medium.

To characterize material inhomogeneity and predict the FEXT of real striplines, an approach for extracting the Dk values of the core and prepreg is presented in [6], in which a trace thickness of zero is assumed [6, Figure 5]. Thus, the cross-section of the inhomogeneous dielectrics is divided into two “layers,” namely, the core and prepreg layers. The simulated data obtained from this two-layer (2L) model can deliver the correct polarity and a reasonable magnitude for stripline FEXT in the time domain. A three-layer (3L) model considering the resin-pocket layer is suggested in [5], which can model the FEXT with slightly improved accuracy and can be connected to the 2L-model via the superposition method. However, a method for extracting $Dk_{resin-pocket}$ is not given in [5], which may limit the application of this algorithm.

As indicated in Figure 1, a real PCB stripline commonly consists of multiple inhomogeneous dielectric layers (IDLs) assembled from several plies of glass fibers. Assuming a 2L or 3L cross-section may simplify the material inhomogeneity in stripline

FEXT analysis because the elements of the per-unit-length capacitance can be well defined [6]. However, the Dk values of woven glass and resin cannot be estimated using either the 2L or 3L model, which prevents engineers from effectively controlling Dk_{core} and $Dk_{prepreg}$ to achieve the minimum FEXT noise in their designs. In addition, several important factors that may influence the stripline FEXT cannot be identified using the existing methods, such as the location of the glass fibers and glass fiber thickness.

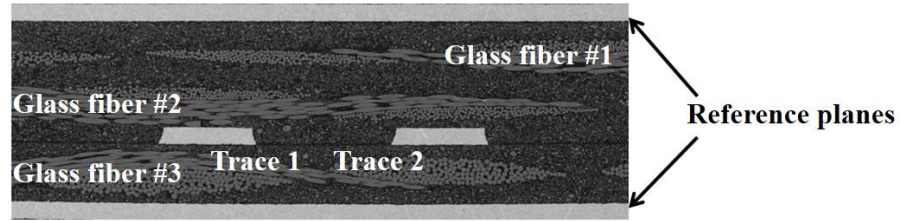


Figure 1. Cross-sectional image of two coupled single-ended striplines, obtained by scanning electron microscopy.

This paper focuses on a novel approach that provides a comprehensive view for studying IDLs. The problem of material inhomogeneity in PCBs is addressed through the proposed algorithm that characterizes the effective Dk values of the “glass layers” and “resin layers.” A good correlation between the simulated and measured data for both FEXT magnitude and transmission phase is reached; moreover, the proposed model can predict the effect on FEXT when the cross-sectional geometries vary and can estimate Dk_{core} and $Dk_{prepreg}$ based on extracted Dk_{glass} and Dk_{resin} values through analytical expressions

2. REPRESENTATION OF IDLS WITH GLASS AND RESIN LAYERS

The stripline cross-section exhibited in Figure 1 can be represented by equivalent glass and resin layers, as shown in Figure 2. Compared with the 2L and 3L models, which are illustrated in Figure 3(a) and (b), the number of IDLs increases significantly, and more dielectrics with different Dk values are utilized to describe the material inhomogeneity. In addition, the resin pocket region in the 3L model is expanded to accommodate the actual configuration.

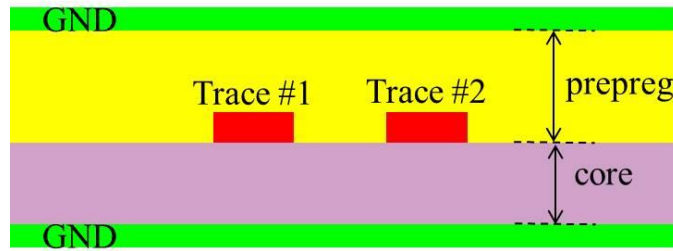
Because glass fibers are impregnated into the epoxy resin during the PCB lamination process [10], the glass layers are defined as such: the thickness of each woven glass determines the upper and lower boundaries of a single glass layer, which contains both glass and resin materials. Owing the fact that the Dk values of various glass fibers are not identical, the equivalent dielectric permittivities of the glass layers are different and are denoted by ϵ_{gn} , where $n = 1, 2, 3$, as shown in Figure 2. It is assumed that the resin is uniformly “distributed” in the regions formed by the resin layers, which is a reasonable assumption if the retained resin content percent is high [2].



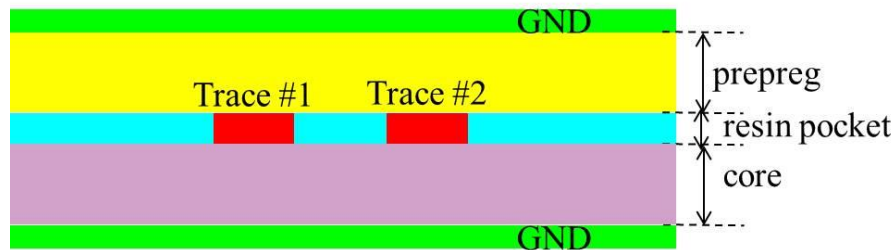
Figure 2. Representation of the stripline cross-section shown in Figure 1 using equivalent glass and resin layers.

3. CALCULATIONS OF DK VALUES OF CORE AND PREPREG

Assuming a typical single-ended stripline with the cross-section shown in Figure 4, two additional models can be constructed with known cross-sectional geometries and material properties, as illustrated in Figure 5(a) and (b). Both of the models are vertically balanced; for instance, the geometry of the prepreg is flipped down to create a symmetrical cross-section in model B. The trace thickness in model A is zero or can be ignored. By contrast, the trace thickness is doubled in model B.



(a) 2L model



(b) 3L model

Figure 3. Existing models for describing material inhomogeneity and predicting stripline FEXT.

Under the statistical condition, the electric potential $\varphi(\beta, y)$ in model A is governed by Poisson's equation [11][12]:

$$\frac{\partial^2 \varphi(\beta, y)}{\partial y^2} = -\frac{\rho(\beta, y)}{\epsilon_0}. \quad (1)$$

where $\rho(\beta, y)$ is the distribution of electric charge density after the Fourier transformation; and ϵ_0 is the permittivity of air. The general solution of Poisson's equation is a linear combination of $e^{\beta y}$ and $e^{-\beta y}$ [11].

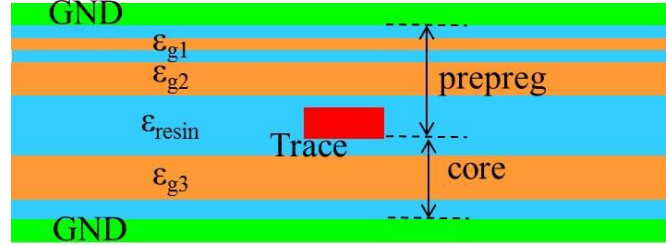


Figure 4. Cross-section of a single-ended stripline with inhomogeneous materials.

The thickness of each layer in model A and the associated electric potentials are indicated in Figure 5(a). Solving for the unique solution requires the following boundary and continuity conditions

$$\phi_1(\beta, y)|_{y=0} = 0. \quad (2a)$$

$$\phi_1(\beta, y)|_{y=a} = \phi_2(\beta, y)|_{y=a}. \quad (2b)$$

$$\epsilon_1 \frac{\partial \phi_1(\beta, y)}{\partial y} |_{y=a} = \epsilon_2 \frac{\partial \phi_2(\beta, y)}{\partial y} |_{y=a}. \quad (2c)$$

$$\phi_2(\beta, y)|_{y=a+b} = \phi_3(\beta, y)|_{y=a+b}. \quad (2d)$$

$$\epsilon_2 \frac{\partial \phi_2(\beta, y)}{\partial y} |_{y=a+b} = \epsilon_3 \frac{\partial \phi_3(\beta, y)}{\partial y} |_{y=a+b}. \quad (2e)$$

$$\phi_3(\beta, y)|_{y=a+b+c} = \phi_4(\beta, y)|_{y=a+b+c}. \quad (2f)$$

$$\varepsilon_3 \frac{\partial \phi_3(\beta, y)}{\partial y} \Big|_{y=a+b+c} = \varepsilon_4 \frac{\partial \phi_4(\beta, y)}{\partial y} \Big|_{y=a+b+c} + \frac{\rho(\beta)}{\varepsilon_0}. \quad (2g)$$

$$\phi_4(\beta, y)|_{y=\infty} = 0. \quad (2h)$$

The line capacitance can be obtained after solving for φ using

$$\frac{1}{C_{core}} = \frac{1}{2\pi} \int_{-\infty}^{\infty} f(\beta) \cdot d\beta. \quad (3a)$$

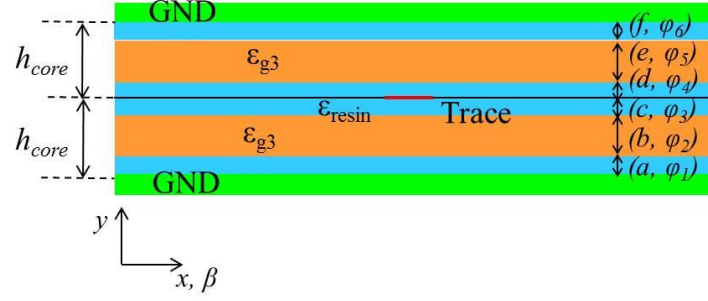
$$f(\beta) = \cosh(\beta a) \cosh(\beta b) \frac{\sinh(\beta c)}{h(\beta) \varepsilon_0} + \frac{\varepsilon_{g3}}{\varepsilon_{resin}} \sinh(\beta a) \sinh(\beta b) \frac{\sinh(\beta c)}{h(\beta) \varepsilon_0} + \frac{\varepsilon_{resin}}{\varepsilon_{g3}} \cosh(\beta a) \sinh(\beta b) \frac{\cosh(\beta c)}{h(\beta) \varepsilon_0} + \sinh(\beta a) \cosh(\beta b) \frac{\cosh(\beta c)}{h(\beta) \varepsilon_0}. \quad (3b)$$

$$h(\beta) = \varepsilon_{resin} \cosh(\beta a) \cosh(\beta b) \cosh(\beta c) + \varepsilon_{g3} \sinh(\beta a) \sinh(\beta b) \cosh(\beta c) + \frac{\varepsilon_{resin}^2}{\varepsilon_{g3}} \cosh(\beta a) \sinh(\beta b) \sinh(\beta c) + \varepsilon_{resin} \sinh(\beta a) \cosh(\beta b) \sinh(\beta c) + \varepsilon_{resin} g(\beta) \cdot q(\beta) \quad (3c)$$

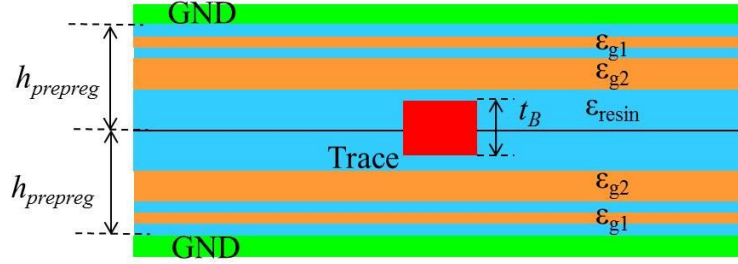
$$g(\beta) = \cosh(\beta a) \cosh(\beta b) \sinh(\beta c) + \frac{\varepsilon_{g3}}{\varepsilon_{resin}} \sinh(\beta a) \sinh(\beta b) \sinh(\beta c) + \frac{\varepsilon_{resin}}{\varepsilon_{g3}} \cosh(\beta a) \sinh(\beta b) \cosh(\beta c) + \sinh(\beta a) \cosh(\beta b) \cosh(\beta c) \quad (3d)$$

$$q(\beta) = \coth(\beta d) - \frac{2\varepsilon_{resin} \varepsilon_{g3} \tanh(\beta f) \sinh(2\beta e) + 4\varepsilon_{resin}^2 \sinh^2(\beta e)}{m(\beta)}. \quad (3e)$$

$$m(\beta) = \varepsilon_{resin} \varepsilon_{g3} \tanh(\beta f) \sinh(2\beta e) \sinh(2\beta d) + 2\varepsilon_{resin}^2 \sinh^2(\beta e) \sinh(2\beta d) + 4\varepsilon_{g3}^2 \sinh^2(\beta d) \cosh^2(\beta e) \tanh(\beta f) + 2\varepsilon_{g3} \varepsilon_{resin} \sinh^2(\beta d) \sinh(2\beta e) - 4\varepsilon_{g3}^2 \sinh^2(\beta d) \tanh(\beta f) \quad (3f)$$



(a) Model A, which is constructed based upon the known material and geometrical parameters for Dk_{core} determination.



(b) Model B, which is constructed based upon the known material and geometrical parameters for $Dk_{prepreg}$ determination. The trace thickness t_B is twice the original value.

Figure 5. Two additional models created for determining Dk_{core} and $Dk_{prepreg}$ based on Dk_{glass} and Dk_{resin} .

Because the line capacitance is proportional to the effective dielectric constant, Dk_{core} can be computed from

$$Dk_{core} = \frac{C_{core}}{C_{air}}. \quad (4)$$

where C_{air} is the corresponding capacitance when all dielectrics are replaced with air.

$Dk_{prepreg}$ can be deduced in a similar fashion. The impact of trace thickness on the calculated $Dk_{prepreg}$ is negligible [11][12].

4. EXTRACTION OF DK VALUES OF GLASS AND RESIN

The modal-based analysis models stripline FEXT through the superposition of odd- and even-modes received at the far-end of the victim line [6]-[9]. The measured common- and differential-mode S-parameters are used to extract Dk_{core} and $Dk_{prepreg}$ from the analytical expressions [6]:

$$Dk_{core} = \frac{0.5 \cdot C_{cc} \cdot (C_{self,pg}^a + 2|C_{g,pg}^a|) - 2 \cdot C_{dd} \cdot C_{self,pg}^a}{C_{self,co}^a (C_{self,pg}^a + 2|C_{g,pg}^a|) - C_{self,pg}^a (C_{self,co}^a + 2|C_{g,co}^a|)} = M. \quad (5)$$

$$Dk_{prepreg} = \frac{0.5 \cdot C_{cc} \cdot (C_{self,co}^a + 2|C_{g,co}^a|) - 2 \cdot C_{dd} \cdot C_{self,co}^a}{C_{self,pg}^a (C_{self,co}^a + 2|C_{g,co}^a|) - C_{self,co}^a (C_{self,pg}^a + 2|C_{g,pg}^a|)} = N. \quad (6)$$

where the definitions of the capacitance components, $C_{self,co}^a$, $C_{self,pg}^a$, $C_{g,co}^a$, and $C_{g,pg}^a$, and the solutions are available in [6]. The modal capacitances are indicated as C_{cc} and C_{dd} , and the subscripts represent the common- and differential-modes, respectively. Their values can be calculated from

$$C_{cc} = \left(\frac{\beta_{cc}}{\omega} \right)^2 \cdot \frac{1}{L_{cc}} = 2(Dk_{prepreg} \cdot C_{self,pg}^a + Dk_{core} \cdot C_{self,co}^a). \quad (7)$$

$$C_{dd} = \left(\frac{\beta_{dd}}{\omega} \right)^2 \cdot \frac{1}{L_{dd}}. \quad (8)$$

In (7) and (8), $\beta_{(cc,dd)}$ is the modal-based phase constant, and $L_{(cc,dd)}$ is the modal inductance, which can be obtained through 2D simulations.

Based on (7), $Dk_{prepreg}$ can be represented by Dk_{core} through

$$Dk_{prepreg} = \frac{\frac{C_{cc}}{2} - Dk_{core} \cdot C_{self,co}^a}{C_{self,pg}^a}. \quad (9)$$

Inserting (9) into (6) and adding (5) and (6) yields

$$Dk_{core} \left(1 - \frac{C_{self,co}^a}{C_{self,pg}^a}\right) + \frac{C_{cc}}{2 \cdot C_{self,pg}^a} = M + N. \quad (10)$$

Therefore, a goal function can be created, and a non-linear fitting approach is utilized to obtain ε_{resin} and ε_{g3}

$$f_{goal_1} = \left| Dk_{core}(\varepsilon_{resin}, \varepsilon_{g3}) \left(1 - \frac{C_{self,co}^a}{C_{self,pg}^a}\right) + \frac{C_{cc}}{2 \cdot C_{self,pg}^a} - M - N \right|. \quad (11)$$

Another goal function is established for the extraction of ε_{g1} and ε_{g2} :

$$f_{goal_2} = |Dk_{preg}(\varepsilon_{g1}, \varepsilon_{g2}) - N|. \quad (12)$$

Knowing the types of glass fibers integrated in the stripline is highly recommended for the extraction of Dk_{glass} and Dk_{resin} , as the outputs of the non-linear fitting can be regarded as best estimates if the fitting range has reasonable boundaries.

It is worth noting that the technique developed here has potential for constructing a design database with the dielectric permittivities of various glass fibers incorporated. Furthermore, engineers can predict stripline FEXT with the estimated dielectric properties and cross-sectional geometries using the proposed model.

5. MEASUREMENT-BASED VALIDATION

To validate the proposed method, a real testing vehicle was fabricated, on which high-precision SMA (SubMiniature version A) connectors were mounted. The two-line structures were built (10 inches and 2 inches), such that the electrical performances of the device under test could be exposed after the 2x-thru de-embedding [13][14]. The S-

matrix measurements were conducted using a Keysight N5244A four-port network analyzer with precision coaxial cables, and the modal insertion losses are exhibited in Figure 6. The measured cross-section of the coupled single-ended traces is illustrated in Figure 7, and the dimensions, $h_1 \sim h_8$, are presented in Table 1.

To compute C_{cc} and C_{dd} , a 2D simulation was performed using ANSYS Q2D [15] to obtain L_{cc} and L_{dd} . According to the datasheet, all of the glass fibers are E-type and have a nominal dielectric constant of 6.5 at 1 GHz. The fitting range for the Dk values of glass layers #1-#3 was set to 5.0-6.6. The extracted Dk values at 1 GHz are summarized in Table 2. It is assumed that the loss tangent is the same for different IDLs. At 1 GHz, the loss tangent is 0.0041, as determined using the approach documented in [16]. The impact of copper surface roughness was modeled using the Huray model [17].

A full-wave simulation was performed in ANSYS HFSS. The comparison of time-domain FEXT between the simulated and measured data is shown in Figure 8, which indicates good agreement. The incident signal had a magnitude of 1 V and a rise time of 35 ps.

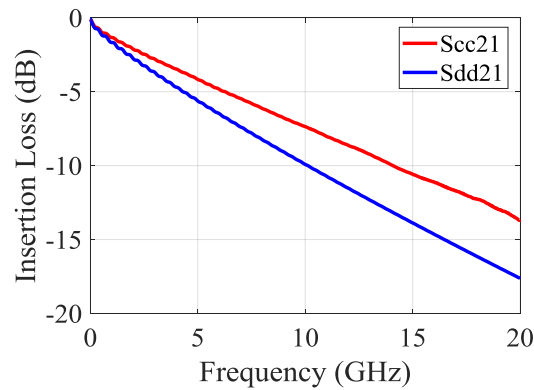


Figure 6. Measured modal S-parameters (insertion loss).

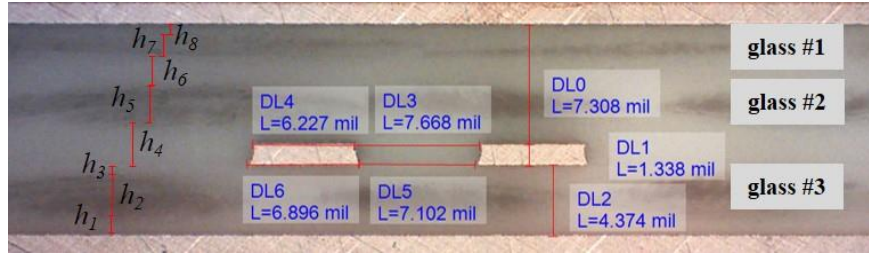


Figure 7. Cross-section of the testing vehicle.

Table 1. Thickness of Glass and Resin Layers

h_1	1.138 mil	h_5	2.459 mil
h_2	2.702 mil	h_6	1.692 mil
h_3	0.534 mil	h_7	0.935 mil
h_4	2.864 mil	h_8	0.696 mil

Table 2. Extracted Dk Values at 1 GHz

Dk_{core}	4.08	Dk_{glass1}	5.62
$Dk_{prepreg}$	3.66	Dk_{glass2}	5.70
Dk_{resin}	2.84	Dk_{glass3}	5.86

6. IMPACT OF GEOMETRICAL PARAMETERS ON STRIPLINE FEXT

The impact of various geometrical parameters on stripline FEXT can be investigated using the proposed model. Here, specific interests are imposed to study the influence of the position and thickness of the glass layer in the prepreg.

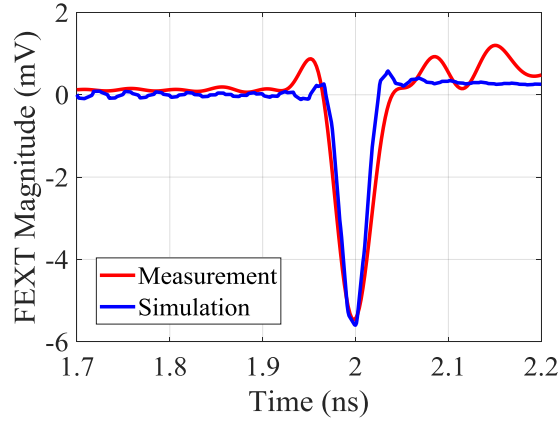


Figure 8. Comparison of time-domain FEXT.

6.1. EFFECT OF GLASS LAYER POSITION ON FEXT

Because the core material is fully cured and its thickness does not vary after PCB lamination [2], a simplified 2D simulation based on the proposed model with multi-layer IDLs was created in ANSYS Q2D, as demonstrated in Figure 9, with the geometries and material properties given in Tables 3 and 4, respectively. In this setup, a single glass layer is incorporated in the prepreg, and its vertical location is manipulated to reveal the impact of position on the simulated FEXT in the time domain. The length of the coupled traces is 8 inches.

The impact of the glass layer location in the prepreg on stripline FEXT is illustrated by the comparison shown in Figure 10. Clearly, the FEXT magnitude changes significantly. In addition, when $h_1 = 1.0 \text{ mil}$, the polarity flips from positive to negative. Unfortunately, the dimension h_1 may not be well controlled in real PCB manufacturing processes due to the ability of current technologies, which may introduce variations in FEXT during the high-volume production phase.

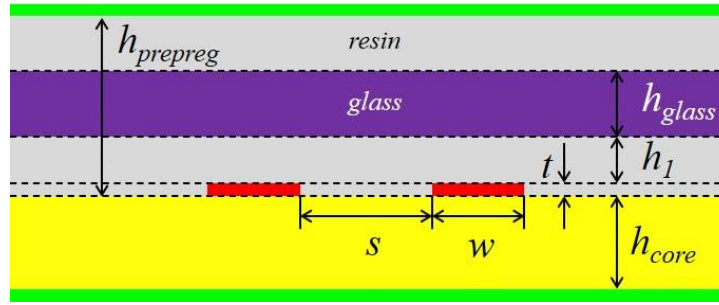


Figure 9. 2D model used to study the impact of glass layer location on stripline FEXT.

Table 3. Cross-Sectional Geometries in Figure 9

$h_{prepreg}$	7.0 mil
h_{core}	4.0 mil
s	6.0 mil
t	1.2 mil
w	5.0 mil
h_{glass}	4.0 mil
h_1	Changes from 0.4 mil to 1.0 mil in 0.1-mil steps in different simulations

Table 4. Material Properties in Figure 9

$Dk_{resin} @ 1 \text{ GHz}$	2.8
$Dk_{glass} @ 1 \text{ GHz}$	5.2
$Dk_{core} @ 1 \text{ GHz}$	3.2
$Df @ 1 \text{ GHz}$	0.005
Copper surface	smooth

6.2. EFFECT OF GLASS LAYER THICKNESS ON FEXT

Another set of 2D simulations was conducted, in which h_1 was fixed to 1.0 mil. h_{glass} was set to 3.9 mil, 3.7 mil, and 3.5 mil in different models. The influence of the variation in glass layer thickness on the simulated FEXT is displayed by the comparison exhibited in Figure 11.

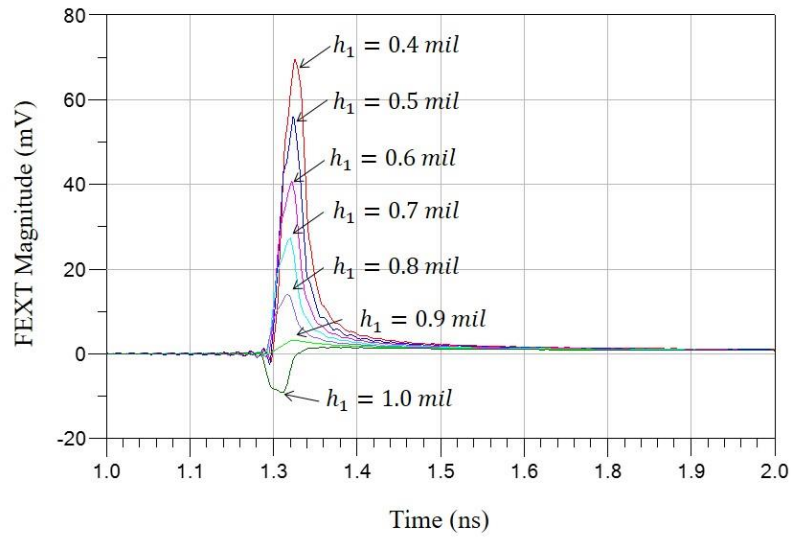


Figure 10. Comparison of simulated FEXT in the time domain when the glass layer location is swept.

Because Dk_{glass} is much larger than Dk_{resin} according to Table 4, the effective $Dk_{prepreg}$ decreases for a thinner glass layer, and the difference between $Dk_{prepreg}$ and Dk_{core} also decreases, which results in a smaller FEXT magnitude [6]. However, the simulated single-ended TDR impedances are almost identical, as demonstrated in Figure 12, indicating that the FEXT magnitude is sensitive to deviations in glass layer thickness.

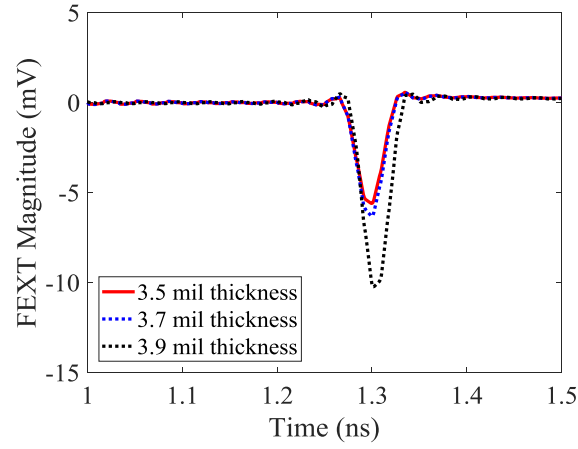


Figure 11. Comparison of simulated FEXT in the time domain for varying glass layer thickness.

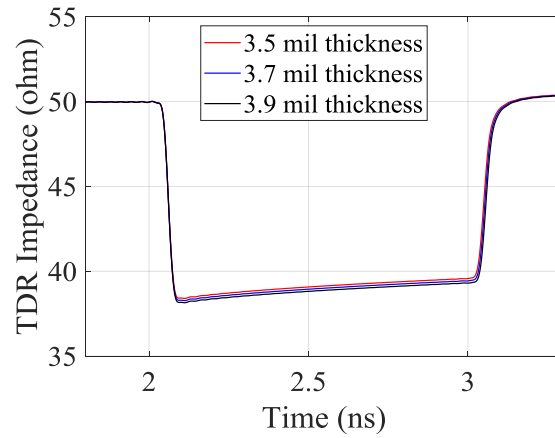


Figure 12. Comparison of simulated TDR impedance for varying glass layer thickness.

7. CONCLUSION

This paper proposes a novel method for the extraction of Dk_{glass} and Dk_{resin} that can provide a comprehensive view of material inhomogeneity in a typical PCB stripline. Good agreement between the measured and modeled FEXT was achieved in the time

domain. The prediction approach based on analytical expressions for Dk_{core} and $Dk_{prepreg}$ is also presented. For the first time, the position and thickness of the glass layers in the prepreg are shown to have observable impacts on stripline FEXT using the proposed model. In addition, the stripline FEXT is more sensitive to the glass layer thickness than to the TDR impedance.

REFERENCES

- [1] S. H. Hall and H. L. Heck, Advanced Signal Integrity for High-Speed Digital Designs. Hoboken, NJ, USA: Wiley, 2009.
- [2] Y. Guo et al., "Far-End Crosstalk Control Strategy for High-Volume High-Speed PCB Manufacturing: The Concept of Critical Resin Content Percent," 2021 IEEE International Joint EMC/SI/PI and EMC Europe Symposium, 2021, pp. 820-824.
- [3] Y. Guo et al., "Robust Extended Unterminated Line (EUL) Crosstalk Characterization Techniques for High-Speed Interconnect," 2020 IEEE International Symposium on Electromagnetic Compatibility & Signal/Power Integrity (EMCSI), 2020, pp. 155-157.
- [4] S. Yong, V. Khilkevich, X. Cai, C. Sui, B. Sen and J. Fan, "Comprehensive and Practical Way to Look at Far-End Crosstalk for Transmission Lines With Lossy Conductor and Dielectric," in IEEE Transactions on Electromagnetic Compatibility, vol. 62, no. 2, pp. 510-520, April 2020.
- [5] Y. Liu et al., "Far-End Crosstalk Analysis for Stripline with Inhomogeneous Dielectric Layers (IDL)," 2021 IEEE International Joint EMC/SI/PI and EMC Europe Symposium, 2021, pp. 825-830.
- [6] S. Yong et al., "Prepreg and Core Dielectric Permittivity ($\epsilon_{\rm r}$) Extraction for Fabricated Striplines' Far-End Crosstalk Modeling," in IEEE Transactions on Electromagnetic Compatibility.
- [7] E. Bracken, "Improved formulas for crosstalk coefficients," in Proc. DesignCon, 2016.

- [8] C. R. Paul, "Literal solutions for time-domain crosstalk on lossless transmission lines," in IEEE Transactions on Electromagnetic Compatibility, vol. 34, no. 4, pp. 433-444, Nov. 1992.
- [9] W. Jiang, X. -D. Cai, B. Sen and G. Wang, "Equation-Based Solutions to Coupled, Asymmetrical, Lossy, and Nonuniform Microstrip Lines for Tab-Routing Applications," in IEEE Transactions on Electromagnetic Compatibility, vol. 61, no. 2, pp. 548-557, April 2019.
- [10] Laminate and Prepreg Manufacturing, public slides from Isola Group Inc. Available at www.Isola-group.com.
- [11] E. Yamashita, "Variational Method for the Analysis of Microstrip-Like Transmission Lines," in IEEE Transactions on Microwave Theory and Techniques, vol. 16, no. 8, pp. 529-535, August 1968.
- [12] E. Yamashita and R. Mittra, "Variational Method for the Analysis of Microstrip Lines," in IEEE Transactions on Microwave Theory and Techniques, vol. 16, no. 4, pp. 251-256, April 1968.
- [13] B. Chen et al., "Differential S-Parameter De-embedding for 8-Port Network," 2018 IEEE Symposium on Electromagnetic Compatibility, Signal Integrity and Power Integrity (EMC, SI & PI), 2018, pp. 52-56.
- [14] B. Chen, J. He, Y. Guo, S. Pan, X. Ye and J. Fan, "Multi-Ports (2^n) $2\times$ -Thru De-Embedding: Theory, Validation, and Mode Conversion Characterization," in IEEE Transactions on Electromagnetic Compatibility, vol. 61, no. 4, pp. 1261-1270, Aug. 2019.
- [15] Y. Guo et al., "Limitations of First-Order Surface Impedance Boundary Condition and Its Effect on 2D Simulations for PCB Transmission Lines," 2020 IEEE International Symposium on Electromagnetic Compatibility & Signal/Power Integrity (EMCSI), 2020, pp. 422-427.
- [16] S. Yong et al., "Dielectric Loss Tangent Extraction Using Modal Measurements and 2-D Cross-Sectional Analysis for Multilayer PCBs," in IEEE Transactions on Electromagnetic Compatibility, vol. 62, no. 4, pp. 1278-1292, Aug. 2020.
- [17] S. Yong et al., "A Cross-sectional Profile Based Model for Stripline Conductor Surface Roughness," 2020 IEEE International Symposium on Electromagnetic Compatibility & Signal/Power Integrity (EMCSI), 2020, pp. 334-339.

SECTION

2. CONCLUSIONS

This dissertation presented the modeling methodologies for both signal integrity and electromagnetic interference, which can be applied to the high-speed channels and modules on an autonomous vehicle. The proposed motor modeling method is feasible for any three-phase motors, as it uses S-parameters for characterization. The approach for glass-weave skew estimation is able to handle complex structures where both glass and epoxy resin are involved. The extraction of the Dk values of glass and resin provides engineers with more information about material inhomogeneity, allowing them to control far-end crosstalk both in the design and massive production phases.

BIBLIOGRAPHY

- [1] J. Zhou et al., "Measurement Techniques to Identify Soft Failure Sensitivity to ESD," in *IEEE Transactions on Electromagnetic Compatibility*, vol. 62, no. 4, pp. 1007-1016, Aug. 2020.
- [2] J. Zhou et al., "IEC 61000-4-2 ESD test in display down configuration for cell phones," *2016 IEEE International Symposium on Electromagnetic Compatibility (EMC)*, 2016, pp. 713-718.
- [3] Y. Guo, S. Jin, X. Sun and J. Fan, "Noise Coupling Mechanism Analysis and Mitigation Method for Receiver Sensitivity Improvement in an Optical QSFP Transceiver Module," *2020 IEEE International Symposium on Electromagnetic Compatibility & Signal/Power Integrity (EMCSI)*, 2020, pp. 502-506.
- [4] S. Penugonda et al., "Reduction of Mode Conversion of Differential-Mode Noise to Common-Mode Noise by Printed Circuit Board Modification for Unbalanced EMI Filter Network," *2021 IEEE International Joint EMC/SI/PI and EMC Europe Symposium*, 2021, pp. 261-264.
- [5] Y. Guo et al., "High-Frequency Modeling of Permanent Magnet Synchronous Motor Considering Internal Imbalances," *2021 Asia-Pacific International Symposium on Electromagnetic Compatibility (AP EMC)*, 2021, pp. 1-3.
- [6] Y. Guo et al., "Far-End Crosstalk Control Strategy for High-Volume High-Speed PCB Manufacturing: The Concept of Critical Resin Content Percent," *2021 IEEE International Joint EMC/SI/PI and EMC Europe Symposium*, 2021, pp. 820-824.
- [7] Y. Guo et al., "The Simulated TDR Impedance In PCB Material Characterization," *2021 IEEE International Joint EMC/SI/PI and EMC Europe Symposium*, 2021, pp. 831-834.
- [8] Y. Liu et al., "Far-End Crosstalk Analysis for Stripline with Inhomogeneous Dielectric Layers (IDL)," *2021 IEEE International Joint EMC/SI/PI and EMC Europe Symposium*, 2021, pp. 825-830.
- [9] B. Pu, J. He, A. Harmon, Y. Guo, Y. Liu and Q. Cai, "Signal Integrity Design Methodology for Package in Co-packaged Optics Based on Figure of Merit as Channel Operating Margin," *2021 IEEE International Joint EMC/SI/PI and EMC Europe Symposium*, 2021, pp. 492-497.
- [10] S. Yong et al., "A Cross-sectional Profile Based Model for Stripline Conductor Surface Roughness," *2020 IEEE International Symposium on Electromagnetic Compatibility & Signal/Power Integrity (EMCSI)*, 2020, pp. 334-339.

- [11] Y. Guo, B. Chen, X. Sun, X. Ye, J. Hsu and J. Fan, "Study of TDR Impedance for Better Analysis to Measurement Correlation," *2019 Joint International Symposium on Electromagnetic Compatibility, Sapporo and Asia-Pacific International Symposium on Electromagnetic Compatibility (EMC Sapporo/APEMC)*, 2019, pp. 88-91.
- [12] X. Sun et al., "Causality Analyzing for Transmission Line with Surface Roughness," *2019 IEEE International Symposium on Electromagnetic Compatibility, Signal & Power Integrity (EMC+SIPI)*, 2019, pp. 516-521.
- [13] Y. Guo et al., "Robust Extended Underminated Line (EUL) Crosstalk Characterization Techniques for High-Speed Interconnect," *2020 IEEE International Symposium on Electromagnetic Compatibility & Signal/Power Integrity (EMCSI)*, 2020, pp. 155-157.
- [14] Y. Guo et al., "Limitations of First-Order Surface Impedance Boundary Condition and Its Effect on 2D Simulations for PCB Transmission Lines," *2020 IEEE International Symposium on Electromagnetic Compatibility & Signal/Power Integrity (EMCSI)*, 2020, pp. 422-427.
- [15] B. Chen, J. He, Y. Guo, S. Pan, X. Ye and J. Fan, "Multi-Ports (2ⁿ) 2×-Thru De-Embedding: Theory, Validation, and Mode Conversion Characterization," in *IEEE Transactions on Electromagnetic Compatibility*, vol. 61, no. 4, pp. 1261-1270, Aug. 2019.
- [16] X. Zhu et al., "I-V Method Based PDN Impedance Measurement Technique and Associated Probe Design," *2019 IEEE International Symposium on Electromagnetic Compatibility, Signal & Power Integrity (EMC+SIPI)*, 2019, pp. 30-33.
- [17] B. Chen et al., "Differential S-Parameter De-embedding for 8-Port Network," *2018 IEEE Symposium on Electromagnetic Compatibility, Signal Integrity and Power Integrity (EMC, SI & PI)*, 2018, pp. 52-56.

VITA

Yuandong Guo was born in Sanmenxia, Henan Province, China. He received the Bachelor's degree in Automation from Beijing Institute of Technology, Beijing, China, in 2006. Then he joined China Electronic Product Reliability and Environmental Testing Institute, Guangzhou, Guangdong, China, as an EMC engineer until 2016. He joined the EMC Laboratory in Missouri University of Science and Technology (formerly, University of Missouri–Rolla), in 2017, and received his Ph.D. degree in Electrical Engineering in July 2022. His research interests included signal and power integrity in high-speed digital design, and electromagnetic modeling in electric vehicles.

After the completion of his Ph. D degree program, he joined Cruise LLC as a Senior Signal Integrity Engineer. Yuandong Guo won the 1st Place in Student EMC Hardware Design Competition from 2021 IEEE EMC & SIPI Symposium.